

RESEARCH

Open Access



Human iPSC-derived pericyte-like cells carrying APP Swedish mutation overproduce beta-amyloid and induce cerebral amyloid angiopathy-like changes

Ying-Chieh Wu¹, Šárka Lehtonen^{1,2*}, Kalevi Trontti¹, Riitta Kauppinen¹, Pinja Kettunen¹, Ville Leinonen^{3,4}, Markku Laakso⁴, Johanna Kuusisto^{4,5}, Mikko Hiltunen⁶, Iiris Hovatta⁷, Kristine Freude⁸, Hiramani Dhungana¹, Jari Koistinaho^{9,10*} and Taisia Rolova^{1*}

Abstract

Background Patients with Alzheimer's disease (AD) frequently present with cerebral amyloid angiopathy (CAA), characterized by the accumulation of beta-amyloid (A β) within the cerebral blood vessels, leading to cerebrovascular dysfunction. Pericytes, which wrap around vascular capillaries, are crucial for regulating cerebral blood flow, angiogenesis, and vessel stability. Despite the known impact of vascular dysfunction on the progression of neurodegenerative diseases, the specific role of pericytes in AD pathology remains to be elucidated.

Methods To explore this, we generated pericyte-like cells from human induced pluripotent stem cells (iPSCs) harboring the Swedish mutation in the amyloid precursor protein (APP^{swe}) along with cells from healthy controls. We initially verified the expression of classic pericyte markers in these cells. Subsequent functional assessments, including permeability, tube formation, and contraction assays, were conducted to evaluate the functionality of both the APP^{swe} and control cells. Additionally, bulk RNA sequencing was utilized to compare the transcriptional profiles between the two groups.

Results Our study reveals that iPSC-derived pericyte-like cells (iPLCs) can produce A β peptides. Notably, cells with the APP^{swe} mutation secreted A β 1-42 at levels ten-fold higher than those of control cells. The APP^{swe} iPLCs also demonstrated a reduced ability to support angiogenesis and maintain barrier integrity, exhibited a prolonged contractile response, and produced elevated levels of pro-inflammatory cytokines following inflammatory stimulation. These functional changes in APP^{swe} iPLCs correspond with transcriptional upregulation in genes related to actin cytoskeleton and extracellular matrix organization.

*Correspondence:

Šárka Lehtonen

sarka.lehtonen@uef.fi

Jari Koistinaho

jari.koistinaho@helsinki.fi

Taisia Rolova

taisia.rolova@helsinki.fi

Full list of author information is available at the end of the article



© The Author(s) 2024. **Open Access** This article is licensed under a Creative Commons Attribution-NonCommercial-NoDerivatives 4.0 International License, which permits any non-commercial use, sharing, distribution and reproduction in any medium or format, as long as you give appropriate credit to the original author(s) and the source, provide a link to the Creative Commons licence, and indicate if you modified the licensed material. You do not have permission under this licence to share adapted material derived from this article or parts of it. The images or other third party material in this article are included in the article's Creative Commons licence, unless indicated otherwise in a credit line to the material. If material is not included in the article's Creative Commons licence and your intended use is not permitted by statutory regulation or exceeds the permitted use, you will need to obtain permission directly from the copyright holder. To view a copy of this licence, visit <http://creativecommons.org/licenses/by-nc-nd/4.0/>.

Conclusions Our findings indicate that the APP_{swe} mutation in iPLCs mimics several aspects of CAA pathology in vitro, suggesting that our iPSC-based vascular cell model could serve as an effective platform for drug discovery aimed to ameliorate vascular dysfunction in AD.

Keywords Pericytes, Vascular dysfunction, Alzheimer's disease, Cerebral amyloid angiopathy, iPSCs

Background












Alzheimer's disease (AD) is a progressive neurodegenerative disorder that accounts for 60–70% of dementia cases. Familial AD is caused by gene mutations in the amyloid precursor protein (*APP*) or presenilin-1 and -2 (*PSEN1/2*) genes [1] that enhance brain deposition of beta-amyloid ($A\beta$) peptides resulting in amyloid pathology. While most cases of AD are sporadic, investigating familial AD can offer valuable insights, as both familial and sporadic AD share similar pathological features.

Although AD research has focused chiefly on neurons, neuronal function largely depends on cerebral blood flow (CBF), providing an adequate supply of oxygen and glucose. Recent imaging studies suggest that hypoperfusion is one of the earliest disease-associated changes in the AD brain, promoting cognitive impairment independently from parenchymal amyloid deposition [2–4]. Cerebral amyloid angiopathy (CAA), the accumulation of $A\beta$ in brain vasculature, is considered a fundamental underlying cause of vascular dysfunction in AD, and it is also a risk factor for hemorrhagic stroke [5]. Pericytes and smooth muscle cells (SMCs) are mural cells that wrap around brain capillaries and form arterial vessel walls, respectively. They play an essential

role in vascular stability and CBF regulation [6]. CAA promotes the degeneration of endothelial cells, pericytes and SMCs and compromises the integrity of the blood–brain barrier (BBB) [5, 7, 8]. A single-nucleus RNA-sequencing analysis of AD patient brains showed that AD risk genes are highly expressed in vasculature-associated cell types [9]. Similar findings emerged in the aged mouse brain, where vascular cells exhibited senescent phenotypes or displayed increased expression levels of AD risk genes [10].

To address the impact of genetic mutations associated with familial AD on pericyte function, we generated pericyte-like cells (iPLCs) from three human iPSC lines carrying the KM670/671NL mutation in *APP* (APP_{swe}), along with seven control lines from healthy individuals (Table 1). Our iPLCs express characteristic pericyte markers, promote a formation of complex tube structure in iPSC-derived endothelial cells (iECs) and decrease iEC layer permeability, thus demonstrating several normal pericyte functions. However, the presence of APP_{swe} mutation impaired the pericyte functions. Therefore, human iPSC-derived vascular cells have the potential to serve as a model for investigating vascular dysfunction in neurodegenerative diseases.

Table 1 iPSC lines used in this study

Represent symbol	Cell line	Sex	Age at Biopsy	APP genotype	APOE genotype	Status when sample taken	References
	Ctrl1	F	77	Control	$\epsilon 3/\epsilon 3$	Healthy	Figure S1
	Ctrl2	F	77	Control	$\epsilon 3/\epsilon 3$	Healthy	Figure S1
	Ctrl3	F	30	Control	$\epsilon 3/\epsilon 3$	Healthy	[11]
	Ctrl4	M	63	Control	$\epsilon 3/\epsilon 3$	Healthy	[12]
	Ctrl5	M	66	Control	$\epsilon 3/\epsilon 3$	Healthy	[13]
	Ctrl6	M	64	Control	$\epsilon 3/\epsilon 3$	Healthy	[14]
	Ctrl7	M	64	Control	$\epsilon 3/\epsilon 4$	NPH w/o amyloid pathology	Figure S1
	Ctrl iAstrocyte	F	44	Control	$\epsilon 3/\epsilon 3$	Healthy	[15]
	AD1	F	58	APP _{swe}	$\epsilon 3/\epsilon 3$	AD	[16]
	AD2	F	30	APP _{swe}	$\epsilon 3/\epsilon 3$	Pre-symptomatic AD	[17]
	AD3	M	15–19	APP _{swe}	$\epsilon 3/\epsilon 4$	Healthy control introduced APP _{swe}	[18]

Materials and methods

Patients and iPSCs

AD iPSC lines were generated from two individuals harboring the APP_{swE} mutation: AD1 was diagnosed with AD, while AD2 was pre-symptomatic without a clinical diagnosis. The third APP_{swE} line, AD3, was generated by introducing KM670/671NL mutation in a healthy male individual using CRISPR-Cas9 [18] and was kindly provided to us by Dr. Kristine Freude. We used altogether six controls from healthy male and female individuals in this study. To reduce the complexity of the genetic background and investigate the phenotype developing from the APP_{swE} mutation, the selected controls (Ctrl1-6) and APP_{swE} mutation (AD1-2) individuals were all carrying apolipoprotein (APOE) $\epsilon 3/\epsilon 3$, the AD risk-neutral allele. However, AD3 was carrying $\epsilon 3/\epsilon 4$ as its parental line. Therefore, we introduced Ctrl7, which carried the APOE $\epsilon 3/\epsilon 4$ allele and came from a patient diagnosed with normal pressure hydrocephalus (NPH) without amyloid pathology, as an additional control for AD3 (Table 1). All iPSC lines expressed pluripotency markers, exhibited a normal karyotype, and could form embryoid bodies and differentiate into three germ layers. The iPSC lines included in individual experiments are listed in Table S1.

Generation and maintenance of iPSCs

Dermal biopsies were collected with informed consent and approval from the Committee on Research Ethics of Northern Savo Hospital District (license no. 123/2016). Fibroblasts were expanded as described previously [19]. Then, somatic cells were reprogrammed to iPSCs with CytoTune-iPS 2.0 Sendai Reprogramming Kit (Thermo Fisher Scientific) as described [11]. Ctrl1 and Ctrl2 lines were reprogrammed at the Biomedicum Stem Cell Centre core facility, University of Helsinki, using CRISPR activators [20, 21]. Briefly, fibroblasts were detached as single cells from the culture plates with TrypLE Select (Gibco, Thermo Fisher Scientific) and electroporated using the Neon transfection system (Invitrogen, Thermo Fisher Scientific) using CRISPRa plasmids [20]. Electroporated fibroblasts were plated on Matrigel-coated plates (growth factor reduced; Corning; 1:200) immediately after the transfections. The medium was changed every other day, and on day 4, the fibroblast medium was changed to a 50:50 ratio of fibroblast medium and stem cell medium (DMEM/F12 with 1% GlutaMAX supplemented with 20% KnockOut Serum Replacement, 0.0915 mM 2-mercaptoethanol, 1% Non-Essential Amino Acids (NEAA; all from Gibco, Thermo Fisher Scientific), 6 ng/mL basic fibroblast growth factor (bFGF; Merck), and 0.25 mM NaB). iPSCs were maintained on Matrigel-coated plates in Essential 8 Medium (E8; Gibco, Thermo Fisher Scientific). 0.5 mM EDTA (Thermo Fisher Scientific) was used

to detach the cells while passaging, and 5 μ M Y27632 ROCK inhibitor (Selleckchem) was applied into the culture to enhance attachment when thawing.

Differentiation of iPLCs

The iPLCs differentiation protocol was adapted from Blanchard et al., 2020 [22] with slight modifications. On day 0, iPSCs were dissociated to single cells by StemPro Accutase (Thermo Fisher Scientific) and replated on Matrigel-coated plates at a density of 2×10^4 cells/cm² in E8 medium with 10 μ M Y27632. On day 1, the medium was switched to N2B27 medium (1:1 DMEM/F12 and Neurobasal medium supplemented with 1% GlutaMAX, 2% B-27, 1% N2 (all from Gibco, Thermo Fisher Scientific), 100 μ g/ml Primocin (InvivoGen), and 50 μ M 2-mercaptoethanol (Merck)) supplemented with 25 ng/mL bone morphogenetic protein (BMP)-4 (PeproTech, Thermo Fisher Scientific) and 8 μ M CHIR99021 (Cayman Chemical) for 4 days for mesoderm specification. The medium was changed every other day. On day 5, the medium was switched to N2B27 medium supplemented with 10 ng/mL platelet-derived growth factor (PDGF)-BB and 2 ng/mL transforming growth factor (TGF β)-3 (both from PeproTech, Thermo Fisher Scientific) for two days to induce differentiation toward iPLCs. The iPLCs were maintained in N2B27 medium without supplements until Day 21 after the initiation of differentiation. On Day 21–23, the iPLCs were either seeded or collected for experiments. Some pilot experiments were conducted at slightly later time points, but none extended beyond Day 35.

Differentiation of iECs

The iEC differentiation protocol was adapted from K. Wang et al. [23]. Initially, the iPSC lines were transduced with E26 transformation-specific variant (ETV) 2 under the control of a doxycycline-inducible promoter (Tet-On system). iPSCs were seeded in E8 medium with 10 μ M Y27632 at 7×10^3 cells/cm² and incubated overnight. The next day, cells were transduced with 2×10^6 TU/mL of lentivirus in E8 medium for 24 h. Then the virus-containing medium was replaced, and cells were allowed to recover for 72 h before selection with 400 μ g/mL G418 (InvivoGen) for 7 days. The pInducer20-ETV2 plasmid was developed by the Genome Biology Unit, University of Helsinki. Biomedicum Virus Core, University of Helsinki, produced lentivirus particles.

For iECs differentiation, on day 0, iPSCs transduced with ETV2 were dissociated into single cells using StemPro Accutase and plated onto Matrigel-coated plates at a density of 2.2×10^4 cells/cm² in E8 medium supplemented with 10 μ M Y27632. On day 1, the culture medium was changed to S1 medium (DMEM/F12 supplemented with

1% GlutaMAX, 60 $\mu\text{g}/\text{mL}$ L-Ascorbic acid, 0.5% penicillin/streptomycin, and 6 μM CHIR99021. On day 3, the S1 medium was replaced with StemPro medium (StemPro-34 SFM) supplemented with 50 ng/ml vascular endothelial growth factor (VEGF)-A, 50 ng/ml bFGF, 10 ng/ml epidermal growth factor (EGF; all growth factors from PeproTech, Thermo Fisher Scientific), 10 μM SB431542, and 2 μM doxycycline hyclate (BioGems). On day 5, the medium was further changed to Human Endothelial SFM (Thermo Fisher Scientific) supplemented with 5% KnockOut serum replacement (Thermo Fisher Scientific), 10 ng/ml bFGF, 5 ng/ml EGF, and 0.5 ng/ml VEGF-A. Subsequently, the cells were passaged in this medium and used for experiments within one week.

Differentiation of iAstrocytes

The iAstrocytes were differentiated as described [15]. In short, neural induction was achieved by culturing the iPSCs in neural differentiation medium (NDM, 1:1 DMEM/F12 and Neurobasal medium, 1% B-27 without vitamin A, 0.5% N2, 1% GlutaMAX, and 0.5% penicillin/streptomycin (50 IU/50 $\mu\text{g}/\text{mL}$)) supplemented with dual SMAD inhibitors 10 μM SB431542 and 200 nM LDN193189 (both from Merck) for 12 days until rosette-like structures appeared. Then, the medium was switched to NDM supplemented with 20 ng/ml bFGF for 2 to 3 days to expand the rosettes. The areas with rosettes were lifted and cultured in ultra-low attachment plates (Corning) with NDM for two days for sphere formation. Next, spheres were cultured in astrocyte differentiation medium (ADM, DMEM/F12, 1% N2, 1% GlutaMAX, 1% NEAA, 0.5% penicillin/streptomycin, and 0.5 IU/ml heparin (Leo Pharma)) supplemented with 10 ng/ml bFGF and 10 ng/ml EGF (PeproTech; ThermoFisher Scientific). Spheres were cultured in ADM medium for 6 to 9 months to get pure astroglial cultures. To mature astrocyte progenitors before the assay, spheres were dissociated with StemPro Accutase and replated on Matrigel-coated plates in ADM supplemented with 10 ng/ml ciliary neurotrophic factor (CNTF; PeproTech, Thermo Fisher Scientific) and 10 ng/ml BMP-4 for 7 to 10 days.

Differentiation of iNeurons

The iNeurons were obtained using the combination of neurogenin (NGN)2 overexpression with dual SMAD and WNT inhibition as described previously [13]. In short, on day 0, a 60–70% confluent plate of iPSCs transduced with NGN2 under Tet-On promoter was exposed to 2 $\mu\text{g}/\text{mL}$ doxycycline in E8 medium. On day 1, the medium was switched to N2 medium (DMEM/F12, 1 \times N2, 1 \times GlutaMAX, 0.3% glucose) supplemented with

2 $\mu\text{g}/\text{mL}$ doxycycline, dual SMAD inhibitors (100 nM LDN193189, 10 μM SB431542B) and 2 μM WNT pathway inhibitor XAV939 (BioGems). On day 2, the concentration of doxycycline and dual SMAD inhibitors was halved, and 5 $\mu\text{g}/\text{mL}$ puromycin (MP biomedical) was added for the selection of NGN2-transduced cells. After removing puromycin and dead cells on day 3, the differentiation continued in the N2 medium with a full concentration of supplements as on day 1. On day 4, emerging neurons were plated on poly-D-lysine (Thermo Fisher Scientific) and laminin (from a mouse Engelbreth-Holm-Swarm sarcoma; ~1.5 $\mu\text{g}/\text{cm}^2$; Merck)-coated surfaces. The medium was then changed to Neurobasal supplemented with 1% GlutaMAX, 2% B-27, 50 μM NEAA, 0.3% glucose, and neurotrophic factors (10 ng/ml of glial cell-derived neurotrophic factor (GDNF), brain-derived neurotrophic factor (BDNF) and CNTF (all from PeproTech, Thermo Fisher Scientific)). Proliferation was halted on day 7 with an overnight treatment of 10 μM floxuridine (Bio-Techne), and cells matured for three weeks, with medium changes three times weekly.

Immunocytochemistry

Cells were washed with PBS and fixed with 3.7% formaldehyde (Merck) for 20 min at room temperature (RT). Afterward, cells were permeabilized with 0.3% Triton X-100 (Merck) and blocked with 5% normal goat serum (Merck) in PBS for 1 h at RT. Primary antibodies, diluted in PBS with 5% NGS, were applied and incubated overnight at 4 °C. Following three washes with PBS, secondary antibodies were applied and incubated for 1 h at RT. Nuclei were stained with 1 $\mu\text{g}/\text{mL}$ DAPI (Sigma) for 10 min at RT. Primary and secondary antibodies are listed in Table 2. Coverslips were mounted on glass slides using Fluoromount-GTM mounting medium (Thermo Fisher Scientific). Images were visualized by an EVOS microscope (Thermo Fisher Scientific) with 4 \times and 10 \times objectives. Brightness and contrast were adjusted using ImageJ software (National Institutes of Health).

qRT-PCR

Total RNA was extracted from iPSCs, iPLCs, iECs, and iAstrocytes using the RNeasy Mini Kit (Qiagen) following the manufacturer's instructions. RNA concentrations were measured by the SimpliNano Spectrophotometer (Biochrom). RNA was subsequently reverse transcribed to complementary DNA (cDNA) using the Maxima Reverse Transcriptase in the presence of RiboLock RNase Inhibitor, dNTP Mix, and Random Hexamer Primer (all from Thermo Fisher Scientific). mRNA levels were quantified via quantitative RT-PCR using TaqMan assay probes (listed in Table 3) with Maxima Probe/ROX qPCR Master Mix (Thermo Fisher Scientific) on the CFX96

Table 2 Primary and secondary antibodies used for ICC

Target	Dilution	Source	Catalog no
Mouse anti- PDGFR β	1:100	R&D Systems	AF385-SP
Mouse anti-Chondroitin Sulfate Proteoglycan (NG2)	1:100	Merck	MAB2029
Rabbit anti-Actin, α -Smooth Muscle + ACTG2	1:300	Abcam	ab32575
Mouse anti-Oct4	1:400	EMD Millipore	MAB4401
Mouse anti-CD31	1:500	Agilent Dako	M0823
Goat anti-Nanog	1:100	R&D Systems	AF1997
Mouse anti-TRA-1–81	1:200	EMD Millipore	MAB4381
Mouse anti-SSEA4	1:400	EMD Millipore	MAB4304
Mouse anti- α -SMA	1:300	Sigma	A5228
Mouse anti-B -III-tubulin	1:1000	Covance	MMS-435P
Mouse anti-AFP	1:300	Sigma	A8452
Goat anti-Mouse IgG (H + L), Alexa Fluor™ 488	1:300	Thermo Fisher Scientific	A-11001
Goat anti-Rabbit IgG (H + L), Alexa Fluor™ 568	1:300	Thermo Fisher Scientific	A-11011

Table 3 primers assay mixes used for mRNA expression studies

Gene	Identifier	Source
<i>PDGFRB</i>	Hs01019589_m1	TaqMan, Thermo Fisher Scientific
<i>DES</i>	Hs00157258_m1	TaqMan, Thermo Fisher Scientific
<i>LAMA2</i>	Hs00166308_m1	TaqMan, Thermo Fisher Scientific
<i>DLC1</i>	Hs00183436_m1	TaqMan, Thermo Fisher Scientific
<i>PDE7B</i>	Hs01054008_m1	TaqMan, Thermo Fisher Scientific
<i>CD248</i>	Hs00535586_s1	TaqMan, Thermo Fisher Scientific
<i>ACTA2</i>	Hs00426835_g1	TaqMan, Thermo Fisher Scientific
<i>APP</i>	Hs00169098_m1	TaqMan, Thermo Fisher Scientific
<i>LRP1</i>	Hs00233856_m1	TaqMan, Thermo Fisher Scientific
<i>BACE1</i>	Hs01121195_m1	TaqMan, Thermo Fisher Scientific
<i>VEGFA</i>	Hs00900055_m1	TaqMan, Thermo Fisher Scientific
<i>ITGA7</i>	Hs01056475_m1	TaqMan, Thermo Fisher Scientific
<i>COL1A1</i>	Hs00164004_m1	TaqMan, Thermo Fisher Scientific
<i>EDNRA</i>	Hs03988672_m1	TaqMan, Thermo Fisher Scientific
<i>EDNRB</i>	Hs00240747_m1	TaqMan, Thermo Fisher Scientific
<i>NANOG</i>	Hs02387400_g1	TaqMan, Thermo Fisher Scientific
<i>SOX2</i>	Hs01053049_s1	TaqMan, Thermo Fisher Scientific
<i>LIN28A</i>	Hs00702808_s1	TaqMan, Thermo Fisher Scientific
<i>CDH5</i>	Hs00901465_m1	TaqMan, Thermo Fisher Scientific
<i>GAPDH</i>	Hs99999905-m1	TaqMan, Thermo Fisher Scientific

Real-Time PCR System (Bio-Rad). *GAPDH* served as the normalization control. Table 4

Western blot

To track the changes in Erk and Akt phosphorylation after ET-1 treatment, 2×10^5 iPSCs were seeded on Matrigel-coated 4-well plates. One day post-seeding, cells were exposed to 30 nM ET-1. At intervals of 15, 30, 45, 60, and 90 min post-exposure of ET-1, cells were lysed using radioimmunoprecipitation assay buffer (RIPA) with

Halt™ protease inhibitor and Halt™ phosphatase inhibitor cocktails (all from Thermo Fisher Scientific). Protein concentrations were determined by Pierce™ BCA Protein Assay Kit (Thermo Fisher Scientific). Subsequently, 5 μ g of protein per sample were separated under reducing conditions on 10% SDS-PAGE pre-cast gels (Bio-Rad). The proteins were then transferred to polyvinylidene difluoride (PVDF) membranes using the Trans-Blot Turbo™ Transfer Starter System and Midi PVDF kit (both from Bio-Rad). Membranes were blocked for 1 h at RT with 5% non-fat dry milk (NFDM) in Tris-Buffered Saline with 0.05% Tween 20 (TBST). Subsequently, membranes were incubated overnight at 4 °C with primary antibodies diluted in 5% bovine serum albumin (BSA) with 0.02% sodium azide in TBST. After washing in TBST, membranes were incubated with horseradish peroxidase (HRP)-conjugated secondary antibodies for 1 h at RT. Protein bands were visualized using the Pierce™ ECL or Pierce™ ECL Plus Western Blotting Substrate (Thermo Fisher Scientific) and imaged on a G:BOX Chemi imaging system (Syngene). Relative protein levels were quantified with ImageJ and normalized to α -tubulin.

To detect α -SMA and APP protein levels, 1×10^6 cells were replated on Matrigel-coated 6-well plates and lysed the next day in RIPA buffer containing protease inhibitors. For detecting Occludin and ZO-1 proteins, cells were harvested from Transwell inserts using the same lysis protocol. The subsequent steps were as described above, with protein levels normalized to GAPDH.

2D tube formation assay

Black-walled, optically clear-bottom 96-well plates (PerkinElmer) were pre-coated with 50 μ l of Matrigel and incubated at 37 °C for 30 min to allow Matrigel polymerization. Afterward, 3×10^4 iECs and 1×10^4 iPSCs, or

Table 4 Primary and secondary antibodies used for WB

Target	Dilution	Source	Catalo no
Rabbit anti-Phospho-p44/42 MAPK (Erk1/2)	1:1000	Cell Signaling	9101S
Rabbit anti-p44/42 MAPK (Erk1/2)	1:1000	Cell Signaling	9102S
Rabbit anti-Occludin	1:500	Thermo Fisher Scientific	71–1500
Rabbit anti-ZO-1	1:500	Thermo Fisher Scientific	600–401-GU7
Mouse anti- α -Tubulin	1:1000	Cell Signaling	3873S
Mouse anti- α -SMA	1:2000	Sigma	A5228
Mouse anti-APP	1:1000	Sigma	MAB348
Goat anti-Rabbit IgG (H + L), HRP	1:10,000	Thermo Fisher Scientific	A16096
Rabbit anti-mouse IgG –Peroxidase	1:80,000	Merck	A9044

3×10^4 iPLCs for iPLC-only cultures, were stained with 100 nM Calcein AM (Cayman Chemical) for 15 min at 37 °C and seeded on top of the Matrigel layer in a 1:1 mixture of the endothelial medium and N2B27 medium. Images were captured every 2 h using Incucyte S3 (Sartorius) whole well module with 4 \times magnification, phase contrast, and green channel settings. The analysis of total length, number of segments and meshes was performed using images taken 6 h post-replating with ImageJ Angiogenesis Analyzer module. Images were cropped to exclude shadowed regions, and the analyzed area of each image was divided by the total well area to calculate the percentage of the analyzed area relative to the whole well. Results were then multiplied by this percentage to normalize for differences in the regions analyzed.

Permeability assay

iPLCs were seeded at a density of $1.5 \times 10^5/\text{cm}^2$ on basolateral sides of 24-well Transwell inserts (0.4 μm pore size, 0.33 cm^2 growth area; Corning) coated with 100-fold diluted Matrigel. After 24 h, the apical side of the Transwell inserts was coated with 100-fold diluted Matrigel and incubated for 2 h at 37 °C. iECs were then dissociated into single-cell suspensions using StemPro Accutase for 5 min. Following dissociation, iECs were replated on the apical side of Transwell insert membranes at a density of $4.5 \times 10^5/\text{cm}^2$, which worked best in our hands and which is comparable to the densities used by Blanchard and coworkers [22]. Permeability assays were performed 7 days following the replating of iECs. 4 kDa and 70 kDa dextran labeled with Alexa 488, and Texas red fluorophores, respectively (both from Sigma), were diluted in the medium to reach a working concentration of 0.5 mg/mL. Standard curves were established, ranging from 0.5 mg/mL to 160 ng/mL through five-fold serial dilutions. For the assay, 900 μl of fresh medium was added to the bottom chamber, and 300 μl 0.5 mg/mL dextran-medium mixture was introduced to the upper chamber.

After a 1-h incubation at 37 °C, 100 μl of medium was sampled from the bottom well, and the mean fluorescent intensity (MFI) was quantified using the FLUOstar Omega spectrometer (BMG Labtech). The concentrations of dextran on the basolateral side were determined by interpolating MFI values against a pre-established standard curve. Then, the permeability coefficient (P_e) was calculated using a method previously described in the literature [24, 25]. The transferred volume (mL) of dextran, which diffused from the apical to the basolateral chamber, was derived from the initial concentration of dextran on the apical side ($[C]_A$) and the final concentration on the basolateral side ($[C]_B$) of the chamber: transferred volume (mL) = $[C]_B \times V_B / [C]_A$, where V_B represents the volume of the basolateral chamber. The permeability surface-area product (PS), measured in cm^3/sec or mL/sec, was calculated by plotting the transferred volume against the reaction time. The PS values were then divided by the surface area of the Transwell inserts to compute the permeability coefficient (P_e in cm/sec).

A β secretion and uptake

iPLCs were seeded at a density of $1.5 \times 10^5/\text{cm}^2$ on 96-well plates coated with 200-fold diluted Matrigel. Following six days of cultivation without medium change, the medium was collected, and the levels of A β 1-40 and A β 1-42 were quantified using ELISA kits according to the manufacturer's instructions (R&D Systems). Results were normalized to the total protein concentration in the cell lysates, determined by the Pierce BCA protein assay (Thermo Fisher Scientific).

Fluorophore-conjugated A β 1-42 (HiLyte Fluor 488-labeled, AnaSpec) was prepared by reconstituting 0.1 mg in 50 μl of water. Then, the solution was sonicated and further diluted to a 5 μM concentration in N2B27 medium. Cells were incubated with 5 μM of fluorophore-conjugated A β 1-42 in N2B27 medium for 24 h. Following incubation, cultures were washed three

times with PBS to remove any unbound residues. Nuclei were stained using 1 $\mu\text{g}/\text{mL}$ Hoechst (Thermo Fisher Scientific). The percentages of A β 1–42-positive cells were quantified from images taken with the EVOS microscope using a 10 \times objective.

iPLCs contraction assay

The assay protocol was adapted from Neuhaus et al., 2017 [26] and Hibbs et al., 2021 [27] with some modifications. Before seeding the cells, 50 μl of the medium was applied into impedance plates (E-Plate 16, Agilent) coated with 100-fold diluted Matrigel for baseline recording. Subsequently, iPLCs were re-plated onto the plate at a density of $6.25 \times 10^4/\text{cm}^2$ and allowed to adhere for 30 min at RT. Cell attachment was monitored by recording the cell index at 15-min intervals using xCELLigence[®] RTCA (Agilent) until cells reached the confluence before the assay, which typically takes 16 to 30 h. Endothelin-1 (ET-1, Merck) was then introduced to the culture at a final concentration of 10 nM and the cell index was recorded at 15-s intervals for 2.5 h and followed by 15-min intervals for the subsequent 27.5 h. Since ET-1 was reconstituted in water, an additional 0.1% of water (final concentration) in the medium served as vehicle control. The 'cell index' was calculated by software using the cell layer's resistance to electrical current, which reflected the contact area between cells and the well surface. The baseline-normalized cell index was generated by normalizing the raw cell index against the mean index of duplicate vehicle controls and the index at the time point when ET-1 is applied to the well. Data analysis was performed with RTCA Software Pro (Agilent).

Cytokines production detection

The Cytometric Bead Array with human soluble protein flex sets (BD Biosciences) was used to examine cytokines secreted by iPLCs. The medium was collected from wells pre-stimulated with 20 ng/mL tumor necrosis factor (TNF) α and 20 ng/mL interleukin (IL)-1 β (both from PeproTech, Thermo Fisher Scientific) for 24 h. As another stimulant, we tried a combination of 100 ng/ml lipopolysaccharide (LPS; Merck) and 15 ng/ml interferon γ (IFN γ ; PeproTech), which acts as a powerful stimulant on iPSC-derived microglia in our hands [28]. Conditioned medium was diluted 10 times with assay diluent for TNF α and IL-1 β -stimulated samples. 20 μl of samples or standards were incubated with 20 μl beads mixture (75 times dilution) for 1 h at RT, followed by 2 h of incubation after adding 20 μl detection reagent (75 times dilution). Samples were run on BD Accuri[™] C6 Flow Cytometer (BD Biosciences) by detecting around 200 to 300 events for each cytokine. Beads were clustered with 675/25 nm (APC) and 780/60 nm (APC-Cy7) optical filters, and

cytokines were quantified using 585/40 nm (PE) filter. The data were analyzed with the FCAP array (SoftFlow), and the absolute concentration of secreted cytokines was calculated according to each cytokine's standard regression curve.

RNA-sequencing and analysis

iPLCs samples for RNA sequencing (RNA-seq) were harvested on day 21 after differentiation started. The density of cells was evaluated from identical wells ranging from 0.8 to 1.6×10^6 cells per well in 6-well plates to ensure cell confluency was comparable between the lines. Total RNA was extracted using the RNeasy Mini Kit following the manufacturer's manual. DNase (Molecular grade; Thermo Fisher Scientific) was introduced during the RNA isolation procedure to produce DNA-free samples following manufacturer's manual. RNase inhibitor RiboLock was added after the elution step to inhibit RNase activity for better RNA preservation. The RNA quantity and quality were analyzed with TapeStation 4200 (Agilent). The Illumina Stranded Total RNA Prep with Ribo-Zero Plus kit (Illumina) was used to deplete ribosomal RNA and prepare RNA-seq libraries. The libraries were then sequenced with NextSeq500 (Illumina). The total number of reads was over 30 million per sample. The library preparation and sequencing service were provided by the Biomedicum Functional Genomics Unit (FuGu) at the Helsinki Institute of Life Science and Biocenter Finland at the University of Helsinki. For detection of differentially expressed genes (DEG), raw sequence reads were aligned to human genome GRCh.38 and annotated to gene exons by STAR aligner v2.7.8a [29] and HTSeq v0.13.5 [30] with GTF v103, respectively. DEG analysis of APPswe pericytes against healthy control samples were performed using the DESeq2 package in R [31]. With the cutoff settings (FDR < 0.05 and absolute log₂ fold change > 1.5), clustering heatmaps were created with R package heatmap 1.0.12 to show DEGs. In addition, using the same cutoff values, pathway enrichment analyses were done by knowledge-based Ingenuity Pathway Analysis (IPA; Qiagen).

Statistics

Statistical analyses were performed using GraphPad Prism 5.01 and 9.3.1 software (GraphPad Software Inc). Columns were compared with Student's t-test or one-way ANOVA with Dunnett's multiple comparison test. Groups with two variables were analyzed by two-way ANOVA with Bonferroni multiple comparison test. Statistical significance was determined with the p-value < 0.05. All data in the graphs are shown as mean \pm SD.

Results

iPSCs efficiently differentiate into iPLCs

Pericytes were differentiated from human iPSCs (Table 1) via mesodermal route according to a slightly modified protocol by Blanchard and coworkers [22]. Given the lack of markers that can reliably differentiate between pericytes and SMCs, we refer to the generated cells as iPSC-pericyte-like cells (iPLCs) in our study.

Our iPLCs exhibited positive immunoreactivity for mural cell markers platelet-derived growth factor receptor beta (PDGFR β), neural-gial antigen 2, proteoglycan (NG2), and alpha-smooth muscle actin (α -SMA) (Fig. 1A). Additionally, these cells displayed significantly higher expression levels of mural cell-enriched genes [9] *PDGFRB*, *DES*, *LAMA2*, and *PDE7B*, in comparison to undifferentiated iPSCs, iECs, and iAstrocytes) (Fig. 1B). While *DLC1* expression was also elevated in iECs, iPLCs still exhibited a significantly higher expression level than both iPSCs and iAstrocytes. As expected, the cells did not express the pluripotency markers *NANOG*, *LIN28A*, and *SOX2*, nor the endothelial cell marker *CDH5* (Figure S2 A-B). To determine the best timeline to conduct our experiments, we examined the expression levels of pericyte-associated genes in four control lines at days 7, 21, 31, and 50 after the initiation of differentiation. We discovered a gradual rise in the expression of *LAMA2*, *PDE7B*, and another mural cell marker *CD248* until day 31 of the culture period (Fig. 1C). The expression of *PDE7B* increased even further on day 50. In contrast, the expression of SMC-associated genes *DES* and *ACTA2* decreased significantly from day 7 to day 21 (Fig. 1C). *PDGFRB* and *DLC1* gene expression levels remained stable across the analyzed time points (Figure S2 C). These results imply that the cells acquired a pericyte-like identity between day 21 and 31 post-differentiation. To minimize the variation, we chose the time-point of 21–23 days post-differentiation for further experiments.

iPLCs promote angiogenesis and barrier integrity

The regulation of vascular function and morphology depends on the interactions between endothelial cells and vascular mural cells. To explore the angiogenic potential of iPLCs, a 2D tube formation assay was performed. For this purpose, iECs were derived from the Ctrl2 line transduced with ETV2 under the doxycycline-inducible promoter. The expression of ETV2 was induced on day three after the initiation of differentiation. Initially, we evaluated the angiogenic capabilities of iECs and iPLCs independently, finding that neither could form clear tube-like structures on a Matrigel layer when cultured alone (Fig. 1D). The analysis was conducted using the ImageJ Angiogenesis Analyzer, which converts images to binary format and identifies tube-like structures. We used parameters such as segment number, mesh number, and area (Fig. 1E) to determine the complexity of the tube structures. Due to converting pixels to binary, even without visible segments or meshes in iECs or iPLCs cultures, the binary images can still produce pseudo structures with low number counts. Subsequently, we examined the ability of iECs to form tubes when subjected to angiogenic factors. Notably, iECs exposed to an angiogenic cocktail (3 ng/mL VEGF-A, 30 nM sphingosine-1-phosphate (S1P), 3 ng/mL phorbol 12-myristate 13-acetate (PMA) and 2.3 ng/mL bFGF) successfully formed complex tubular structures, with a significant increase in the total mesh area (Fig. 1D, F). The total numbers of master segments and meshes also tended to be increased following the stimulation with the angiogenic cocktail (Fig. 1F). iPLCs-conditioned medium (CM) did not significantly induce tube formation in iECs. However, direct co-culturing of iECs with iPLCs resulted in a significant increase in the numbers of master segments and meshes as well as the total mesh area (Fig. 1D, F). These observations suggest that iPLCs may play a

(See figure on next page.)

Fig. 1 Differentiation and characterization of iPSC-derived pericyte-like cells (iPLCs). **A** Immunostaining for PDGFR β , α -SMA, and NG2 in day 21 iPLCs derived from control lines. Nuclei are stained with DAPI. Scale bars, 100 μ m. **B** Comparison of relative gene expression levels for *PDGFRB*, *DES*, *LAMA2*, *DLC1*, and *PDE7B* among iPLCs, iECs, iAstrocytes, and iPSCs. Expression levels are shown as fold change relative to *GAPDH*. **C** Relative gene expression levels of *LAMA2*, *PDE7B*, *CD248*, *DES*, and *ACTA2* in iPLCs across Day 7, 21, 31, and 50. Expression levels are shown as fold change relative to *GAPDH*. **D** 2D tube formation images showing iECs alone, iPLCs alone, iECs exposed to angiogenic cocktail or iPLC-conditioned medium (CM), and iECs co-cultured with iPLCs. Scale bars, 300 μ m. **E** Illustration of master segments (red arrows) and mesh structures (blue polygon). **F** Statistical analysis of the number of master segments, meshes count, and meshes area. **G** Schematic of the experimental setup for permeability assays. **H** Immunostaining of CD31 and α -SMA on iECs and iPLCs cultured on Transwell inserts. Nuclei are stained with DAPI. Scale bars, 100 μ m. **I** Endothelial permeability coefficients (*Pe*) for 4 kDa and 70 kDa fluorescently labeled dextran across iEC only, iEC bilayers, iECs in co-culture with iPLCs cultures and empty well without cells on inserts as control. **J–K** Western blots for ZO-1 and Occludin from two experimental batches, analyzing iEC-only, iPLC-only, iEC bilayers, and iECs in co-culture with iPLCs. GAPDH served as a loading control (**J**). Statistical analysis depicting fold changes in ZO-1 and Occludin expression levels relative to iEC-only controls for each batch (**K**). The dots indicate the average values of technical replicates for each biological sample (lines, batches), with the color of the dots representing different lines. Except in (**I**), where the dots from empty well represent the data from one well of one experimental batch. The data are presented as mean \pm SD. Statistical analysis utilized one-way ANOVA with Dunnett's multiple comparison test, with significance denoted: **p* < 0.05, ***p* < 0.01, ****p* < 0.001 and *****p* < 0.0001

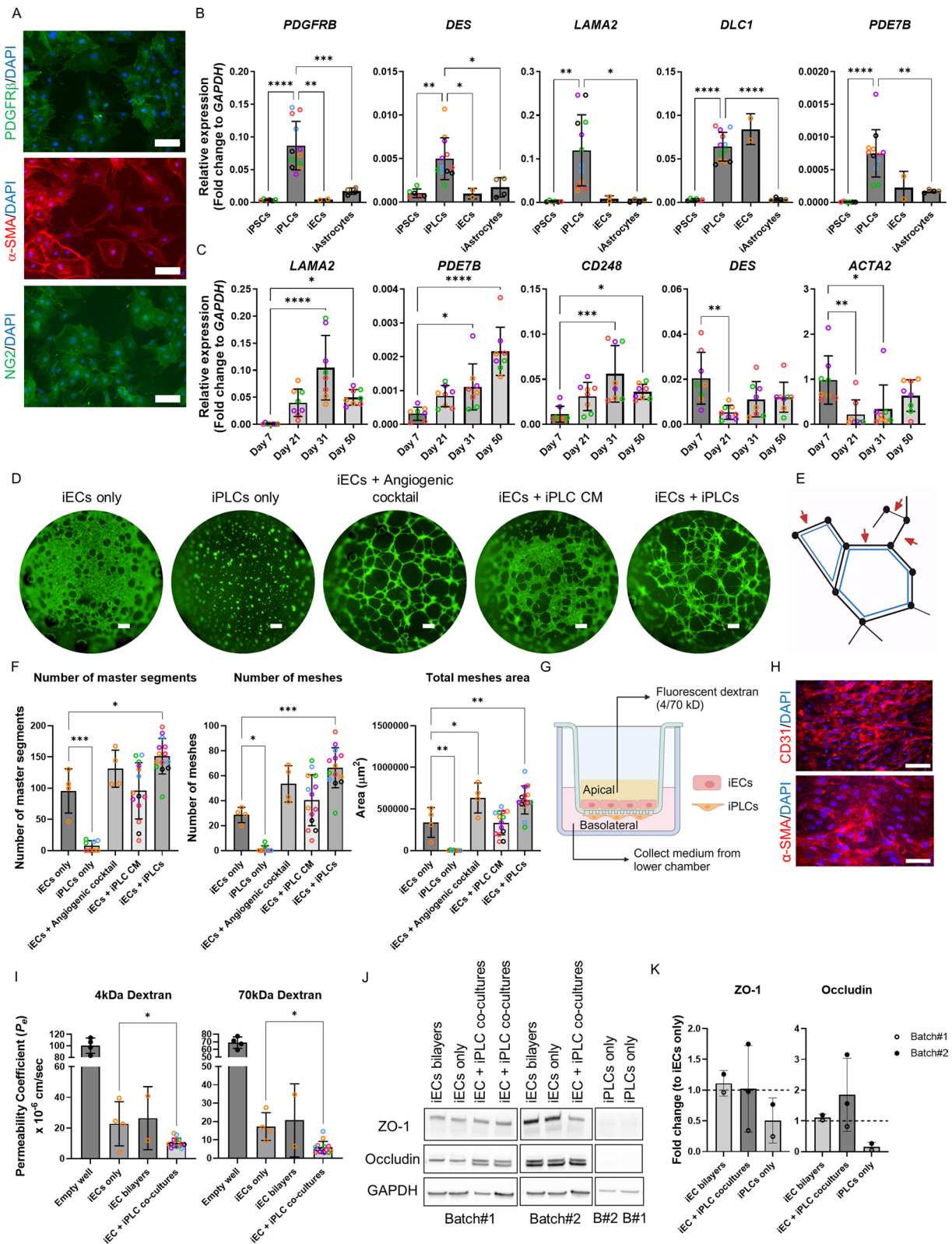


Fig. 1 (See legend on previous page.)

crucial role in promoting vessel formation and stabilization by directly interacting with iECs.

Additionally, the ability of iPLCs to induce BBB properties in iECs was evaluated using a Transwell model. In the experimental setup, iPLCs were seeded on the basolateral side of the inserts, while iECs were cultured on the apical side (Fig. 1G). As controls, iECs grown alone (iECs only) and iECs plated on both apical and basolateral sides (iEC bilayers) were used. Initially, CD31 and α -SMA stainings were conducted to confirm the proper attachment of iECs and iPLCs to the membrane before performing the permeability assay (Fig. 1H). The permeability to 4 kDa and 70 kDa dextran of 7-day-old co-cultures was significantly reduced (Fig. 1I) compared to apical iECs alone. The Western blot analysis showed that the presence of iPLCs did not significantly affect RIPA-soluble levels of the tight junction proteins (TJPs) ZO-1 and occludin as compared to iECs alone (Fig. 1J–K). These findings indicate that iPLCs regulate the formation and integrity of blood vessels, thereby confirming their functional efficacy.

APPswe iPLCs exhibited differential expression of pericyte markers and expressed α -SMA stress fibers

We expanded our investigation to compare the expression of pericyte genes between iPLCs derived from healthy individuals and those carrying APPswe mutation. Our analysis revealed no significant differences in the expression levels of *PDGFRB*, *LAMA2*, *DLC1*, and *CD248* between APPswe and control iPLCs (Fig. 2A). However, a notable reduction in the expression of *PDE7B* and *DES* was observed in APPswe iPLCs, alongside an increase in *ACTA2* expression (Fig. 2B). *ACTA2* encodes for α -SMA, a protein associated with cell contractility, and α -SMA protein levels were also significantly elevated in APPswe iPLCs (Fig. 2C). A detailed analysis of α -SMA staining revealed distinct organizational patterns. In control iPLCs, α -SMA was diffusely distributed and

primarily located at the cell margins. In contrast, in APPswe iPLCs, there was a noticeable increase in the presence of actin stress fibers (Fig. 2D). The quantification of cells exhibiting actin stress fibers revealed a significant increase in the prevalence of these structures among iPLCs with APPswe mutation (Fig. 2D). These findings suggest potential defects in APPswe iPLCs.

iPLCs can produce and secrete A β peptides

The accumulation of A β deposits in the brain is a hallmark of AD. Previous research has reported the co-labeling of pericytes with A β in human AD brain [32, 33]. However, it is not clear whether pericytes actively produce A β or uptake it from the surrounding extracellular space. We found that iPLCs harboring APPswe mutation secreted significantly more A β 1-42 (413.7 ± 88.4 pg/mg cell lysate over 7 days; Fig. 2E) compared to control cells (43.4 ± 54.7 pg/mg cell lysate; Fig. 2E). As expected, iPLCs secreted higher levels of A β 1-40 than A β 1-42 (Controls: 894.2 ± 125.8 pg/mg; APPswe: 3165.4 ± 701.7 pg/mg), and the genotype effect was similar to the effect on A β 1-42 (Fig. 2E). The mRNA level of *BACE1* in both control and APPswe iPLCs was similar to those found in iAstrocytes (Fig. 2F), while the level of *APP* was significantly higher in iPLCs. Notably, APP protein levels were higher in APPswe iPLCs compared to controls (Fig. 2G). Our data suggest that pericytes can produce A β and may contribute to the A β pathology, although the extent of their contribution is yet to be fully understood. To clarify this, we compared A β production by iNeurons, iAstrocytes, and iPLCs to gauge the relative contribution of pericytes to the overall A β pathology. We found that APPswe iPLCs secreted on average 100 times lower levels of both A β 1-42 and A β 1-40 than APPswe iNeurons when grown at the same cell density for 72 h (Fig. 2H). The findings suggest that the contribution of pericytes to total brain amyloid load in AD is limited.

(See figure on next page.)

Fig. 2 APPswe iPLCs displayed altered expression of pericyte markers, α -SMA stress fibers, and amyloid beta pathology. **A–B** Comparative analysis of relative expression levels of *PDGFRB*, *LAMA2*, *DLC1*, *CD248* (**A**), and *PDE7B*, *ACTA2*, *DES* (**B**) between control and APPswe iPLCs. Expression levels are shown as fold change relative to *GAPDH*. **C** Representative blots for α -SMA in control and APPswe iPLCs, using α -tubulin as a loading control. **D** Immunostaining of α -SMA in control and APPswe iPLCs, with nuclei stained by DAPI. Scale bars, 100 μ m. The percentage of cells with stress fibers was quantified using ImageJ's threshold function to measure cell coverage. **E** A β 1-42 and A β 1-40 levels in media from control and APPswe iPLCs, normalized to total protein content. **F** Relative gene expression levels of *APP* and *BACE1* in control and APPswe iPLCs, as well as iAstrocytes, quantified as fold changes relative to *GAPDH*. **G** Western blot for APP in control and APPswe iPLCs, with GAPDH as the loading control. **H** A β 1-42 and A β 1-40 levels measured in media from iPSC-neurons, astrocytes, and iPLCs derived from an APPswe individual. The obtained values were normalized to total protein content. **I** Images of iPLCs internalizing HiLyte 488-labeled A β 1-42, displayed at 4 \times and 10 \times magnifications, scale bar 100 μ m (10 \times). The percentage of cells internalizing A β 1-42 was quantified using 10 \times images. **J** Relative gene expression levels of *LRP1* in control iPLCs, APPswe iPLCs, and iAstrocytes, quantified as fold changes relative to *GAPDH*. The dots indicate the average values of technical replicates for each biological sample (lines, batches), with the color of the dots representing different lines. The data are presented as mean \pm SD. Statistical analysis was performed using one-way ANOVA with Dunnett's multiple comparison test (F, H, J) or t-test (A, B, C, D, E, G, I). The significance levels are denoted as follows: * $p < 0.05$, ** $p < 0.01$, *** $p < 0.001$ and **** $p < 0.0001$

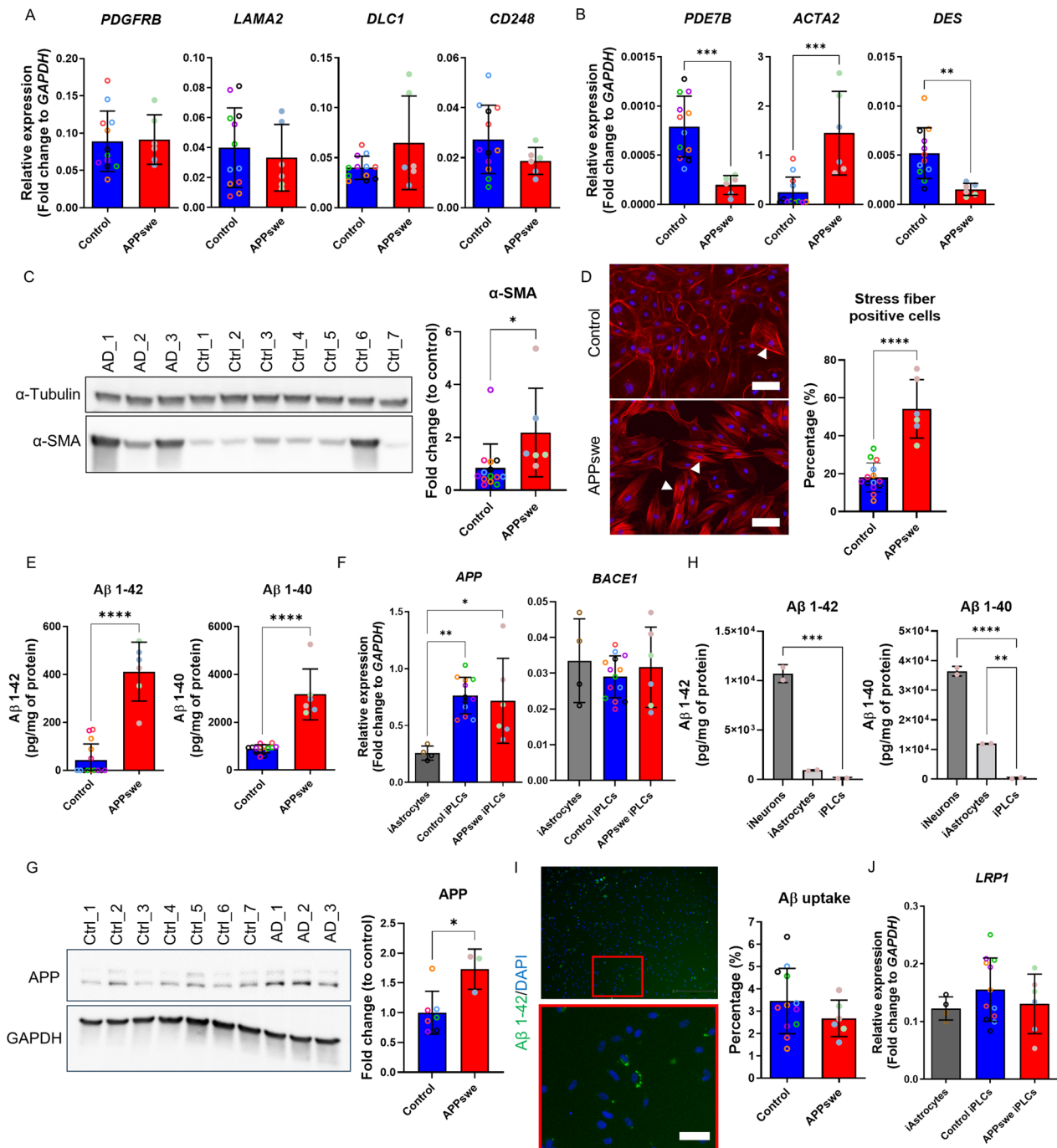


Fig. 2 (See legend on previous page.)

To investigate Aβ uptake potential of our iPLCs, we introduced fluorescently labeled fibrillar Aβ1-42 to the cultures and incubated them for 24 h. Only around 3% of control cells ingested Aβ1-42, and the APPsw mutation did not affect Aβ1-42 uptake (Fig. 2 I). Both control and APPsw iPLCs expressed *LRP1* mRNA levels

similar to iAstrocytes, known to express detectable levels of *LRP1* [34] (Fig. 2). Furthermore, when iPLCs were subjected to pHrodo-conjugated zymosan-coated beads, no uptake of these pathogen-mimicking particles was observed. Thus, it appears that the phagocytic activity of these iPLCs is low.

APPswe mutation significantly altered the transcriptome of iPLCs

To further investigate the impact of the APPswe mutation on iPLCs, we conducted transcriptomic analysis on 21-day-old cells. A pairwise comparison identified 687 differentially expressed genes (DEGs) between APPswe and control iPLCs (Figure S3 A, Table S2), with 257 genes upregulated and 430 downregulated. The top-most up- and downregulated genes in APPswe iPLCs are highlighted in red and blue in volcano plot, respectively (Fig. 3A). We used Ingenuity Pathway Analysis (IPA) to identify the pathways most affected by APPswe mutation in iPLCs (Fig. 3B, C, Table S3). Among the five strongest downregulated pathways, we identified Rho GDP dissociation inhibitor (RHOGDI) signaling, hypoxia inducible factor (HIF)1 α signaling, IL-8 signaling, opioid signaling, and ET-1 signaling (Fig. 3B). The ET-1 pathway regulates vasoconstriction [35] while IL-8 and HIF1 α signaling pathways are involved in angiogenesis, inflammation, and metabolic regulation [36, 37]. The top five upregulated pathways in APPswe iPLCs were associated with actin/cytoskeleton reorganization, including paxillin signaling, actin cytoskeleton signaling, agrin interactions at neuromuscular junction, signaling by RHO family GTPases, and PAK signaling (Fig. 3C). Among the DEGs shared by these pathways, there was a significant number of genes related to myosin chains, smooth muscle actin, and integrins (Fig. 3D, E). Additionally, the DEGs involved in the regulation of angiogenesis included *IL6R* and *KDR* (Fig. 3D). Another pathway enrichment analysis using Pathview revealed significant changes in vascular smooth muscle contraction and cardiomyopathy-related pathways, extracellular-receptor interaction and focal adhesion pathways (Fig. 3F). Detailed examination of genes within these pathways identified *ITGA2*, *ITGA4*, *ITGA6*, and *MYLK*, which are involved in cytoskeleton reorganization as described in IPA analysis (Table S4). Gene ontology analysis further underscored an enrichment in biological processes associated with vascular and muscle functions and extracellular matrix/structure organization (Fig. 3G, Tables S5-7), which are crucial for vascular stability and pericyte fate determination [38].

This analysis also emphasized an enrichment in cellular components of contractile fibers and myofibers (Fig. 3G, Tables S5-7).

In summary, our transcriptomics data suggests that APPswe iPLCs may exhibit altered functionalities such as cell contractility, inflammatory response, and metabolism regulation.

APPswe iPLCs produce higher levels of MCP-1 after inflammatory stimulation

Pericytes can sense inflammatory stimuli and activate innate immune responses, such as the release of pro-inflammatory cytokines and overexpression of adhesion molecules, including intercellular adhesion molecule (ICAM)-1 and vascular cell adhesion molecule (VCAM)-1 [39, 40]. Given that our transcriptome analysis (Fig. 3D) showed a downregulation of IL-8 signaling pathway in APPswe iPLCs, we tested the effect of a 24 h exposure to a combination of proinflammatory cytokines TNF α and IL-1 β (Fig. 4A) on these cells. Following the exposure, inflammatory mediators IL-6 (two-way ANOVA, $p=0.0427$), IL-8 ($p=0.0028$), monocyte chemoattractant protein (MCP)-1 (CCL2) ($p<0.0001$), regulated on activation, normal T cell expressed and secreted (RANTES; CCL5) ($p=0.0267$), and soluble VCAM-1 ($p=0.0156$), were secreted by iPLCs. It is worth noting that bacterial lipopolysaccharide failed to induce this response (Fig. 4A), potentially due to extremely low expression levels of Toll-like receptor (*TLR*) 2 and *TLR4* as well as *CD14* genes (Table S8). Upon stimulation with TNF α and IL-1 β , APPswe iPLCs secreted significantly higher levels of MCP-1 and showed a rising trend in soluble VCAM-1 ($p=0.0517$) compared to control cells (Fig. 4A). No significant genotype effect was observed on the levels of the remaining inflammatory mediators tested. This suggests that APPswe iPLCs are sensitive to inflammatory stimuli, resulting in an increased release of certain pro-inflammatory mediators.

APPswe iPLCs impair angiogenesis and barrier integrity

Given the observed changes in angiogenesis-related gene expression within the APPswe iPLCs transcriptome compared to controls (Fig. 3B), we used tube formation

(See figure on next page.)

Fig. 3 APPswe iPLCs exhibit an altered transcriptome. **A** Volcano plot depicting DEGs between control and APPswe iPLCs (cutoffs: Adjusted p -value < 0.05 and an absolute \log_2 fold change > 1.5). The analysis included seven control and three APPswe lines. **B–C** Ingenuity Pathway Analysis identifying the top 10 canonical pathways that are most significantly downregulated (**B**) and upregulated (**C**) in APPswe iPLCs compared to controls, with pathways selected based on the highest z-scores (p -value < 0.05). **D** List of DEGs related to AD risk from GWAS, angiogenesis and pericyte contraction process (cutoffs: Adjusted p -value < 0.05 and an absolute \log_2 fold change > 1). **E** List of genes involved in RHOGDI, Paxillin and Actin Cytoskeleton signaling pathways. **F** Pathview pathway analysis identifying the top 10 pathways most affected in APPswe iPLCs relative to controls, ranked by the highest enrichment scores. **G** Gene ontology (GO) enrichment analysis revealed pathways enriched in Biological Process, Molecular Function, and Cellular Component in APPswe iPLCs relative to controls

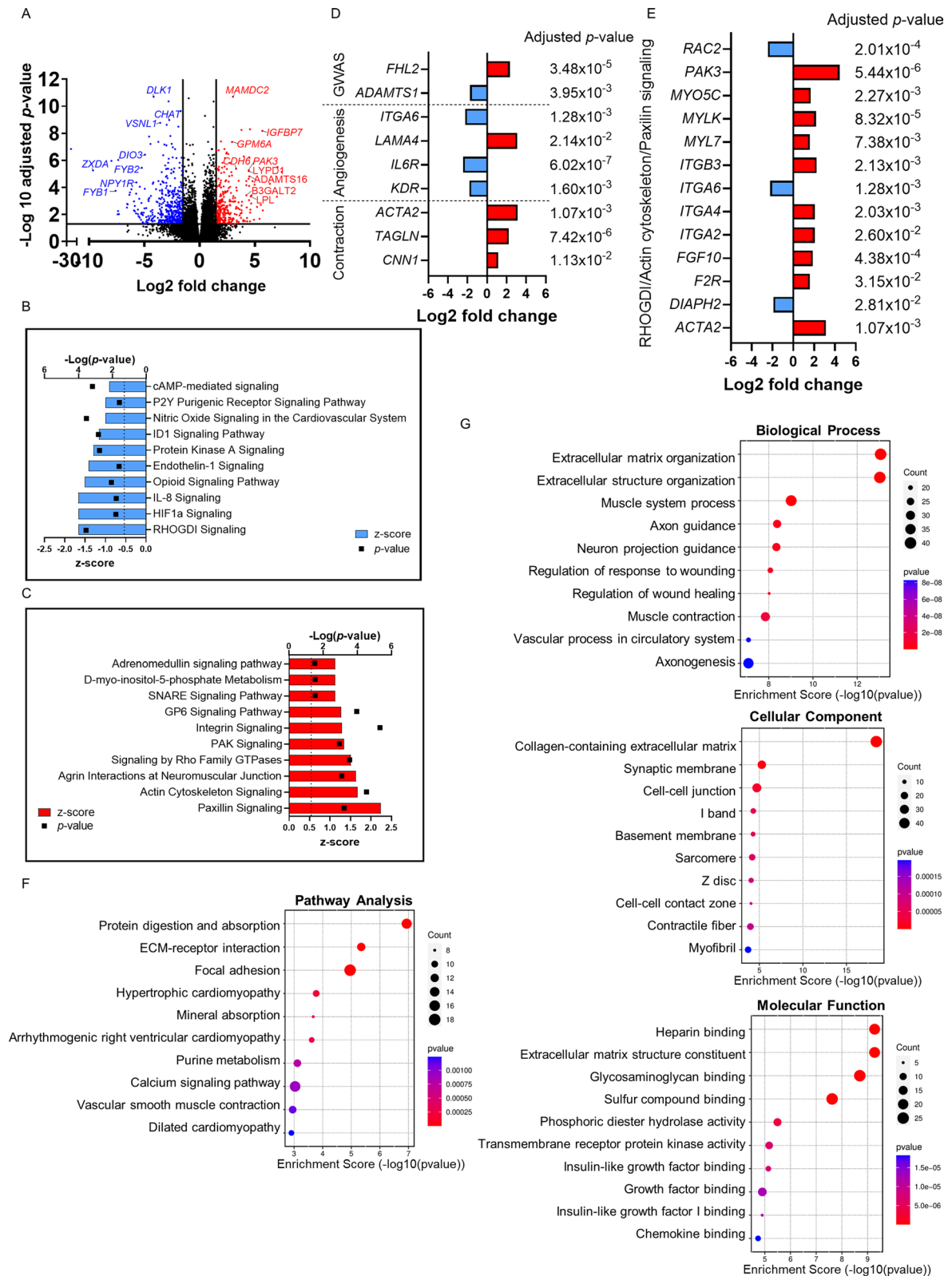


Fig. 3 (See legend on previous page.)

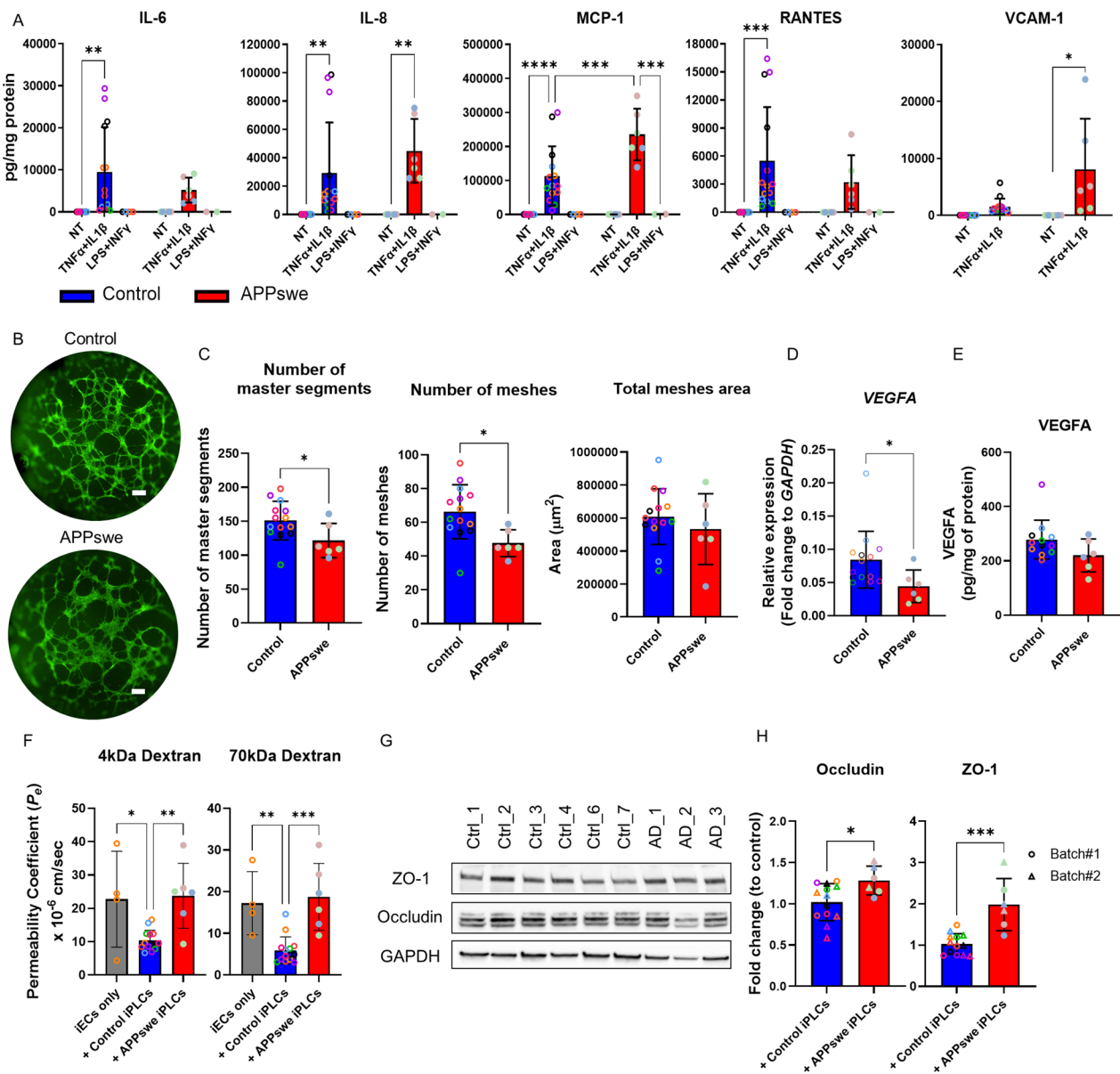


Fig. 4 APPswe iPCLs show functional deficits in responding to inflammation, supporting angiogenesis, and maintaining barrier integrity. **A** IL-6, IL-8, MCP-1, RANTES, and VCAM-1 concentrations were measured in iPLCs culture media after 24 h of stimulation with TNF α and IL-1 β or LPS and IFN γ stimulation. Results were normalized to total protein content. Statistical differences between treatments and genotypes were indicated. **B–C** 2D tube formation assays involved culturing iECs alongside both control and APPswe iPCLs (**B**), scale bars, 300 μ m. Statistical comparisons were made regarding the number of master segments, number of meshes, and mesh area between co-cultures of control and APPswe iPCLs with iECs (**C**). **D** Relative gene expression levels of VEGFA in control and APPswe iPCLs, quantified as fold changes relative to GAPDH. **E** VEGF-A protein levels in lysates from control and APPswe iPCLs were measured and normalized to total protein content. **F** P_e for 4 kDa and 70 kDa fluorescently labeled dextran, assessed in iECs only cultures and iECs in co-culture with either control or APPswe iPCLs. **G** Representative blots of ZO-1 and Occludin from control and APPswe iPCLs, with GAPDH as the loading control. **H** Quantification results from two batches. The dots indicate the average values of technical replicates for each biological sample (lines, batches), with the color of the dots representing different lines. The data are presented as mean \pm SD. Statistical analysis was performed using two-way ANOVA with Bonferroni multiple comparison test (**A**), one-way ANOVA with Dunnett’s multiple comparison test (**F**) or t-test (**C–E, H**). The significance levels are denoted: * p < 0.05, ** p < 0.01, *** p < 0.001 and **** p < 0.0001

and dextran permeability assays to evaluate the ability of APPswe iPCLs to support normal endothelial cell functions. In co-cultures of iECs with APPswe iPCLs,

the network of self-assembled tubes was less complex compared to those formed with control iPCLs (Fig. 4B). Statistical analysis revealed a significant reduction in the

number of segments and meshes in iECs co-cultured with APPswe iPLCs relative to control cells (Fig. 4C). However, no differences were observed in the total mesh area. These results suggest that APPswe iPLCs have a diminished capacity to support angiogenesis. Since VEGF-A is the major stimulator of angiogenesis [41, 42] and *VEGFA* mRNA levels tended to be lower in the transcriptomic dataset (Table S8), we checked the levels of *VEGFA* expression by RT-qPCR (Fig. 4D). Consistent with RNA-seq data, *VEGFA* mRNA levels were reduced in APPswe iPLCs compared to the control group. We then checked the VEGF-A protein levels by ELISA. However, no difference was observed in VEGF-A levels in cell lysates between APPswe and control iPLCs (Fig. 4E), and the secretion of soluble VEGF-A into the culture medium was undetectable for both groups.

Consistent with previous findings, the permeability of iECs to both 4 kDa and 70 kDa fluorescently labeled dextran was notably reduced in co-cultures with control iPLCs, as opposed to iEC-only cultures and co-cultures with iECs on the basolateral side (Fig. 4F). However, permeability significantly increased when iECs were co-cultured with APPswe iPLCs compared to those with control cells, aligning with iEC-only cultures (Fig. 4F). This observation indicates that APPswe iPLCs undermine the integrity of the endothelial barrier. To check whether the degradation of the TJPs could explain these differences, we conducted a Western blot analysis. Surprisingly, the levels of RIPA-soluble ZO-1 and occludin were increased in APPswe pericytes when normalized to GAPDH (Fig. 4G, H), indicating that our results could not be explained by TJP degradation and that further research is needed to understand the underlying mechanisms.

APPswe iPLCs exhibit a prolonged response to ET-1 treatment

Since we had detected a higher prevalence of stress fibers (Fig. 2D) and upregulation of cytoskeleton reorganization pathways in APPswe iPLCs (Fig. 3E–G), we aimed to further investigate potential defects in pericyte contractility. To validate the contractile ability of iPLCs in response to vasoconstricting and vasodilating signals, we exposed our cultures to ET-1 or adenosine triphosphate (ATP), respectively. We then monitored cell contraction process using the xCELLigence system.

This system measures the electric impedance of the cell layer converting it into a cell index that reflects changes in the cell surface area. The iPLCs exhibited immediate contraction in response to ET-1 administration, as shown by a reduction in cell index (Fig. 5A). After the initial contraction, there was an increase in cell index 20–30 min post-ET-1 treatment, suggesting cell

relaxation. In contrast, when ATP was used as a vasodilator, it caused an elevation in the cell index (Fig. 5A), indicating a potential relaxation of the cells. Further analysis of the contraction/relaxation dynamics, as inferred from the slope changes, showed no significant differences between cells exposed to 10 nM and 100 nM of ET-1 (Fig. 5B). Consequently, we chose 10 nM ET-1 for subsequent experiments.

After confirming basic contractile responses, we investigated the behavior of both control and APPswe iPLCs. Compared to the control group, APPswe iPLCs exhibited a steeper contraction slope (Fig. 5C, D). They also required a significantly prolonged recovery period to attain normal cell index (Fig. 5C, D). Next, we assessed the transcriptomics data to determine the expression levels of ET-1 receptors. The iPLCs expressed both *EDNRA* and *EDNRB* genes, but the former was expressed on average 10 times higher than the latter (Table S8). This suggests that endothelin receptor type A may be the primary ET-1 receptor in iPLCs. Nonetheless, there were no significant differences in the expression of these genes between the genotypes. These results were confirmed using RT-qPCR (Fig. 5E). Since ET-1 receptors are G-protein-coupled receptors and extracellular signal-regulated kinase 1 and 2 (Erk1/2) is a common downstream pathway, we collected cells at various time points following ET-1 treatment to observe alterations in downstream signaling. The levels of Erk phosphorylated at Thr202 and Tyr204 (p-Erk) peaked in both control and APPswe iPLCs around 10 min post-treatment, with a decline thereafter (Fig. 5F). Interestingly, the p-Erk/t-Erk ratio at 10 min post-ET-1 treatment increased more in APPswe iPLCs than in controls (Fig. 5H–I). These observations suggest that APPswe iPLCs exhibit a hypercontractile phenotype with prolonged recovery post-ET-1 exposure. However, further research is needed to confirm the significance of the elevated p-Erk/t-Erk ratio.

Discussion

In this study, we generated human iPLCs carrying a genetic variant linked to familial AD. These iPLCs expressed high levels of common pericyte marker genes. Interestingly, some pericyte marker genes such as *PDE7B*, *ACTA2*, and *DES* exhibited differential expression in APPswe iPLCs compared to controls. These changes are more likely caused by intrinsic properties of the APPswe mutation in iPLCs rather than differentiation guidance failures.

A key discovery of our study is a novel mechanism potentially contributing to CAA pathology. Previous studies reported A β production by cerebrovascular cells [43, 44]. However, the significance of these findings has remained ambiguous because A β accumulation in the

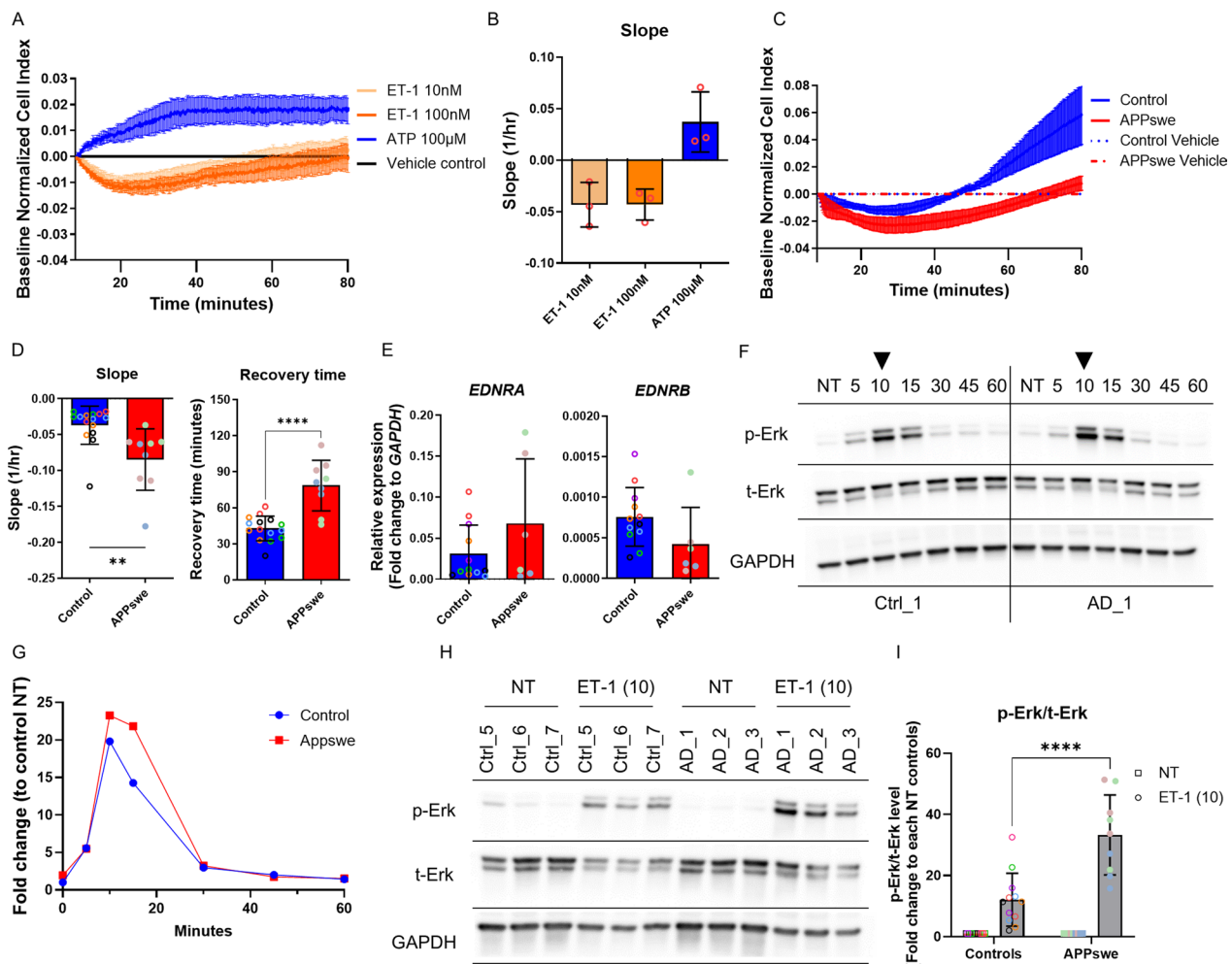


Fig. 5 APPswe iPCLs exhibited a hypercontractile phenotype. **A–B** Electrical impedance measurements evaluated the contractile response of iPCLs to various concentrations of ET-1 and ATP. Response curves, normalized to vehicle control, depicted cell index showing the response (**A**), while the response slope indicated contraction speed post-treatment (**B**). (**C**) Cell index of the contractile response to ET-1 treatment between control and APPswe iPCLs. **D** Statistical analysis of response slope and recovery time for iPCLs returning to normal size. **E** Gene expression levels of *EDNRA* and *EDNRB* in control versus APPswe iPCLs, quantified as fold changes relative to *GAPDH*. **F–G** Time-resolved blots for phosphorylated (p)-Erk and total (t)-Erk in control and APPswe iPCLs post-ET-1 treatment at intervals of 5, 10, 15, 30, 45, and 60 min, as well as in non-treated (NT) cells (**F**), with quantifications normalized to *GAPDH* and control NT wells (**G**). (**H–I**) Blots of p-Erk and t-Erk from control and APPswe iPCLs 10 min after ET-1 treatment and from NT cells, with *GAPDH* serving as the loading control (**H**). Blot quantification was normalized to *GAPDH* levels, and treatment groups were further normalized to the NT wells of their respective lines (**I**). The dots indicate the average values of technical replicates for each biological sample (lines, batches), with the color of the dots representing different lines. The data are presented as mean ± SD. Statistical analysis was performed using two-way ANOVA with Bonferroni multiple comparison test (**I**) or t-test (**D, E**). The significance levels are denoted: * $p < 0.05$, ** $p < 0.01$, *** $p < 0.001$ and **** $p < 0.0001$

vasculature is generally thought to originate predominantly from neurons [45]. Indeed, we see that iPCLs produce substantially lower levels of A β than neurons. However, our findings reveal that APPswe iPCLs produced on average 10 times higher levels of A β 1-42 and 3.5-fold higher levels of A β 1-40 as compared to controls. Given their localization, pericytes may still contribute to vascular amyloidosis.

We also show that APPswe iPCLs have an impaired capacity to support vessel formation, stabilization, and barrier integrity, exhibit a prolonged contractile response, and produce increased levels of pro-inflammatory cytokines upon inflammation.

The hypercontractile phenotype of APPswe iPCLs was accompanied by an increased mRNA expression of *ACTA2*, which encodes for α -SMA, and other

cytoskeleton-regulating proteins. In SMCs, the contractile functions are primarily dependent on contractile proteins such as α -SMA, smooth muscle myosin heavy chains, and calponin [46]. While it's unclear whether pericytes utilize the same contraction mechanisms as SMCs, they are thought to modulate CBF through contraction. Our data also revealed an increase in the prevalence of stress fibers in APPswe iPSCs. Stress fibers are linked with contractile activity in myofibroblasts and cardiomyocytes [47]. SMCs obtained from AD individuals have been reported to express higher levels of contractile proteins [48]. Moreover, Yilmaz-Ozcan and coworkers have demonstrated that a decrease in α -SMA expression levels reduces pericyte contraction in mouse brain [49]. These findings further support the hypothesis that there is a correlation between pericyte contraction and α -SMA expression. Previous publications have also shown that Erk and p38 MAPK pathways regulate myosin light chain phosphatase, thereby contributing to sustained smooth muscle contraction [50, 51]. Our examination of Erk phosphorylation following exposure to vasoconstrictor ET-1 revealed enhanced Erk pathway activation in APPswe iPSCs. This suggests that the hypercontractility phenotype, characterized by a steeper slope and prolonged recovery time, may stem from amplified Erk signaling. However, additional evidence is required to firmly establish this conclusion.

The hypercontractile phenotype observed in APPswe iPSCs may also be linked to A β pathology. A previous study found that the accumulation of A β had a constricting effect on capillaries in patients with cognitive decline by eliciting the ET-1 signaling pathway in pericytes [52]. Similarly, in vitro human pericytes exhibited compromised contraction and relaxation after exposure to exogenous A β [26, 27]. Thus, the hypercontractile phenotype observed in APPswe iPSCs in our model is consistent with prior studies and could potentially cause decreased CBF in patients with AD. The hypercontractile phenotype correlates with elevated expression levels of contractile proteins, amplified Erk signaling, and A β secretion. Further research is required to fully understand the underlying mechanisms.

In dextran permeability studies, APPswe iPSCs exhibited a compromised ability to enhance the tightness of iEC layer. This effect could potentially result in BBB leakage, commonly seen in CAA patients, leading to neuroinflammation and accelerating the progression of AD [53]. However, the total levels of TJPs were higher in APPswe iPSCs. This suggests that the impaired ability of APPswe iPSCs to promote barrier formation cannot be explained by a degradation of the occludin and ZO-1 and may be attributed to differences in iPSC attachment or the involvement of other TJPs and/or signaling pathways.

Moreover, APPswe iPSCs secreted significantly higher levels of the chemokine MCP-1. Overexpression of MCP-1 and VCAM-1 in the endothelium can cause monocytes to adhere strongly to the endothelial layer [54, 55]. This phenomenon has been linked with endothelial barrier dysfunction [56, 57]. Thus, our in vitro models containing APPswe iPSCs successfully replicate some features of CAA.

Angiogenesis plays a crucial role in the development and adulthood. Impaired angiogenesis can decrease vessel density, reduce CBF and nutrient transport, and thus potentially worsen the progression of AD. Previous studies indicated that reduced capillary density may result from both vessel degeneration and insufficient angiogenesis due to a lack of angiogenic factors. To validate the role of iPSCs in vessel formation, we compared iEC cultures alone to those exposed to an angiogenic cocktail and those co-cultured with iPSCs. In our hands, the co-culture with control iPSCs showed a similar enhancement of tube-like structure formation as the cocktail of angiogenic factors, suggesting that iPSCs were able to stimulate angiogenesis. The iPSC-conditioned medium alone did not have the same effect likely because the concentration of angiogenic factors was too low. Indeed, we could not detect the major angiogenic factor VEGF-A in the conditioned medium by ELISA. Nevertheless, iPSCs did produce VEGF-A protein as detected by ELISA in the whole-cell lysates, and we can speculate that locally released VEGF-A and possibly other angiogenic factors can reach sufficiently high levels to promote angiogenesis. We observed that co-cultured iPSCs had an even stronger impact on the number of master segments and meshes compared to the angiogenic cocktail. Our results do not exclude the stabilizing effect of pericytes on newly formed vessels.

Interestingly, APPswe iPSCs induced slightly less complex tube structures than control cells. We identified angiogenesis-related genes that were significantly reduced in APPswe iPSCs at the mRNA level (Fig. 3 D and 4 D), potentially linking them to the observed phenotype. These included *VEGFA* and its receptor *KDR*, *IL6R*, and *ITGA6*. IL-6/IL6R signaling has been reported to regulate endothelial cell proliferation and migration [58–60]. ITGA6 protects established endothelial tubes by regulating CXCR4 expression [61]. Our study reveals transcriptional and functional abnormalities in APPswe iPSCs hindering their ability to support angiogenesis and suggests potential molecular targets for future research.

In conclusion, our study shows that APPswe iPSCs induce CAA-like changes, leading to increased BBB permeability and defective angiogenesis and vasoconstriction in vitro. Utilizing human iPSC-derived models of brain vascular cells may enhance our understanding of

various diseases, including CAA, and help identify critical pathways and develop novel therapies. Given the high prevalence of vascular dysfunction in AD, combination drugs targeting both A β pathology and vascular dysfunction could be a promising therapeutic strategy.

Conclusions

Using the established iPSC protocol, our study reaffirms that these cells express classic *in vivo* pericyte markers. We conducted permeability, angiogenesis, and contraction assays to demonstrate that these cells also replicate *in vivo* pericyte functions. Further, we explored how iPSCs contribute to vascular dysfunction in AD by using lines from individuals with APP^{swe} mutation. Our findings indicate that the APP^{swe} mutation leads to functional defects and transcriptome changes in iPSCs. Notably, altered functions such as impaired barrier integrity, reduced angiogenesis support, and hypercontractility are linked to CAA pathology. This suggests a significant role for pericytes in CAA pathology, potentially exacerbating vessel destabilization and inducing vascular dysfunction in AD. Additionally, our RNA-seq results identified potential pathways that might contribute to these observed phenotypes. As a result, our study has provided an iPSC-derived, human-based platform for drug screening targeting pericytes and/or vascular endothelial cells in the future.

Abbreviations

ATP	Adenosine triphosphate
α -SMA	Alpha-smooth muscle actin
AD	Alzheimer's disease
APP ^{swe}	Swedish mutation in the amyloid precursor protein
APOE	Apolipoprotein E
ADM	Astrocyte differentiation medium
A β	Beta-amyloid
BBB	Blood-brain barrier
CAA	Cerebral amyloid angiopathy
CBF	Cerebral blood flow
DEGs	Differentially expressed genes
Erk	Extracellular signal-regulated kinase (p44/42 MAPK)
ET	Endothelin
bFGF	Fibroblast growth factor 2
HRP	Horseshoe peroxidase
iPSCs	Induced pluripotent stem cells
IPA	Ingenuity Pathway Analysis
ICAM	Intercellular adhesion molecule
IL	Interleukin
iECs	iPSC-endothelial cells
iPLCs	iPSC-pericyte-like cells
MCP-1/CCL2	Monocyte chemoattractant protein 1
NDM	Neural differentiation medium
NG2	Neural-glial antigen 2, proteoglycan
PMA	Phorbol 12-myristate 13-acetate
PDGFR β	Platelet-derived growth factor receptor beta
PVDF	Polyvinylidene difluoride
PSEN1/2	Presenilin-1 and -2
RIPA	Radioimmunoprecipitation assay buffer
RANTES/CCL5	Regulated on activation, normal T cell expressed and secreted
RNA-seq	RNA sequencing
SMCs	Smooth muscle cells
S1P	Sphingosine-1-phosphate

TLR	Toll-like receptor
TJPs	Tight junction proteins
ETV2	Transcription factor E26 transformation-specific variant 2
TNF α	Tumor necrosis factor-alpha
VCAM	Vascular cell adhesion molecule
VEGF	Vascular endothelial growth factor

Supplementary Information

The online version contains supplementary material available at <https://doi.org/10.1186/s12987-024-00576-y>.

Supplementary File 1. Figure 1. Characterization of pluripotency of Ctrl1, Ctrl2 and Ctrl7 iPSC cell lines (A) Representative immunocytochemistry images of OCT4, NANOG, TRA 1-81 and SSEA4 Ctrl1, Ctrl2 and Ctrl7. Scale bars, 100 μ m. (B) Representative karyograms from Ctrl1, Ctrl2 and Ctrl7 showing normal euploid karyotypes (46,XX for Ctrl1, Ctrl2 and 46,XY for Ctrl7).

Supplementary File 2. Figure 2. Pluripotency and endothelial markers are not expressed on iPSCs. (A) The relative gene expression levels of pluripotency markers *NANOG*, *LIN28A* and *SOX2* were compared between iPSCs and iPSCs, quantified as fold changes relative to *GAPDH*. (B) The relative gene expression levels of ECs marker *CDH5* were compared between iECs, iPSCs and iPSCs, quantified as fold changes relative to *GAPDH*. (C) Relative gene expression levels of *PDGFRB* and *DLC1* in iPSCs across Day 7, 21, 31, and 50. Expression levels are shown as fold change relative to *GAPDH*. The dots indicate the average values of technical replicates for each biological sample (lines, batches), with the color of the dots representing different lines. The data are presented as mean \pm SD. Statistical analysis was performed using one-way ANOVA with Dunnett's multiple comparison test. The significance levels are denoted as follows: * $p < 0.05$, ** $p < 0.01$, *** $p < 0.001$ and **** $p < 0.0001$.

Supplementary File 3. Figure 3. DEGs of APP^{swe} versus control iPSCs (A) Heat map depicting DEGs between control and APP^{swe} iPSCs (cutoffs: Adjusted p -value < 0.05 and absolute log₂ fold change > 1.5). The analysis included seven control and three APP^{swe} lines

Supplementary File 4.

Supplementary File 5.

Acknowledgements

We express our gratitude to Anne Nyberg, Agnes Viherä, and Erja Huttu for their valuable assistance in the characterization of iPSCs. Also, we express our gratitude to Dr. Vesa Oikkonen, Minerva Institute, Helsinki, for generously lending us the xCELLigence device, which we utilized to measure pericyte contraction. Additionally, we acknowledge the Biomedicum Functional Genomics Unit (FuGu) at the University of Helsinki for their support in providing bulk RNA-seq services. We extend our gratitude to the Genome Biology Unit, Biomedicum Stem Cell Center and the Biomedicum Virus Core funded by HILIFE (University of Helsinki) and Biocenter Finland for their support in providing plasmid, iPSCs and virus packaging services.

Author contributions

Y.C.W. conducted the majority of experiments, analyzed the data, and wrote the initial draft of the manuscript. K.T. and I.H. performed the normalization of bulk RNA-seq data and conducted the analysis of DEGs. R.K. and H.D. generated doxycycline inducible ETV2 iPSC line. P.K. provided an NGN2 iPSC line. K.F. provided a Swedish mutation iPSC line for the study. T.R. conceptualized the project, provided supervision, and contributed to manuscript revision and comments. Š.L. and J.K. provided valuable input on the manuscript and supervised the project. V.L., M.L., J.Ku. provided patient fibroblasts for the study. All authors have thoroughly reviewed and approved the final version of the manuscript for publication.

Funding

Open Access funding provided by University of Helsinki (including Helsinki University Central Hospital). This project has received funding from the European Union's Horizon 2020 research and innovation program under the Marie Skłodowska-Curie grant agreement No. 813294 (J.K. and Y.C.W.), the

Sigrid Juselius Foundation (J.K.,Š.L. and MH), the Academy of Finland (grant 334525, J.K.; grant 338182, MH; UHBrain Profi 6, T.R.), the Jane and Aatos Erkko Foundation (Š.L.), and the Doctoral program Brain & Mind at the University of Helsinki (Y.C.W.). The funders had no role in the study design, data collection, or interpretation. We declare no competing interests.

Availability of data and materials

The raw sequencing data and metadata are accessible on the EU Open Research Repository (Pilot) in Zenodo, identified by <https://doi.org/10.5281/zenodo.11488682> (<https://doi.org/https://doi.org/10.5281/zenodo.11488682>). Please note that the raw RNA-seq data is kept strictly confidential to uphold patient privacy and confidentiality.

Declarations

Ethics approval and consent to participate

All samples used for generating iPSCs were collected with informed consent and received approval from the Research Ethics Committee of Northern Savo Hospital District (license no. 123/2016).

Consent for publication

Not applicable.

Competing interests

The authors declare no competing interests.

Author details

¹Neuroscience Center, University of Helsinki, 00014 Helsinki, Finland. ²A.I.Virtanen Institute for Molecular Sciences, University of Eastern Finland, 70211 Kuopio, Finland. ³NeuroCenter, Kuopio University Hospital, Kuopio, Finland. ⁴Institute of Clinical Medicine, University of Eastern Finland, Kuopio, Finland. ⁵Department of Medicine and Clinical Research, Kuopio University Hospital, Kuopio, Finland. ⁶Institute of Biomedicine, University of Eastern Finland, Kuopio, Finland. ⁷SleepWell Research Program, Faculty of Medicine, University of Helsinki, Helsinki, Finland. ⁸Department of Veterinary and Animal Sciences, University of Copenhagen, 1870 Frederiksberg, Denmark. ⁹Helsinki Institute of Life Science, University of Helsinki, 00014 Helsinki, Finland. ¹⁰Drug Research Program, Division of Pharmacology and Pharmacotherapy, University of Helsinki, 00014 Helsinki, Finland.

Received: 1 July 2024 Accepted: 13 September 2024

Published online: 27 September 2024

References

- Waring SC, Rosenberg RN. Genome-wide association studies in Alzheimer disease. *Arch Neurol*. 2008. <https://doi.org/10.1001/archneur.65.3.329>.
- Montagne A, Nation DA, Pa J, Sweeney MD, Toga AW, Zlokovic BV. Brain imaging of neurovascular dysfunction in Alzheimer's disease. *Acta Neuropathol (Berl)*. 2016;131(5):687–707.
- Klohs J. An integrated view on vascular dysfunction in Alzheimer's disease. *Neurodegener Dis*. 2019;19(3–4):109–27.
- Hecht M, Krämer LM, Von Arnim CAF, Otto M, Thal DR. Capillary cerebral amyloid angiopathy in Alzheimer's disease: association with allocortical/hippocampal microinfarcts and cognitive decline. *Acta Neuropathol (Berl)*. 2018;135(5):681–94.
- Biffi A, Greenberg SM. Cerebral amyloid angiopathy: a systematic review. *J Clin Neurol*. 2011;7(1):1.
- Kaplan L, Chow BW, Gu C. Neuronal regulation of the blood–brain barrier and neurovascular coupling. *Nat Rev Neurosci*. 2020;21(8):416–32.
- Challa VR, Thore CR, Moody DM, Anstrom JA, Brown WR. Increase of white matter string vessels in Alzheimer's disease. *J Alzheimers Dis*. 2004;6(4):379–83.
- Halliday MR, Rege SV, Ma Q, Zhao Z, Miller CA, Winkler EA, et al. Accelerated pericyte degeneration and blood–brain barrier breakdown in apolipoprotein E4 carriers with Alzheimer's disease. *J Cereb Blood Flow Metab Off J Int Soc Cereb Blood Flow Metab*. 2016;36(1):216–27.
- Yang AC, Vest RT, Kern F, Lee DP, Agam M, Maat CA, et al. A human brain vascular atlas reveals diverse mediators of Alzheimer's risk. *Nature*. 2022;603(7903):885–92.
- Zhao L, Li Z, Vong JSL, Chen X, Lai HM, Yan LYC, et al. Pharmacologically reversible zonation-dependent endothelial cell transcriptomic changes with neurodegenerative disease associations in the aged brain. *Nat Commun*. 2020;11(1):4413.
- Holmqvist S, Lehtonen Š, Chumarina M, Puttonen KA, Azevedo C, Lebedeva O, et al. Creation of a library of induced pluripotent stem cells from Parkinsonian patients. *Npj Park Dis*. 2016;2(1):16009.
- Fagerlund I, Dougalis A, Shakirzyanova A, Gómez-Budia M, Pelkonen A, Kontinen H, et al. Microglia-like Cells promote neuronal functions in cerebral organoids. *Cells*. 2021;11(1):124.
- Kettunen P, Lesnikova A, Räsänen N, Ojha R, Palmunen L, Laakso M, et al. SARS-CoV-2 infection of human neurons requires endosomal cell entry and can be blocked by inhibitors of host phosphoinositol-5 kinase. *Neuroscience*. 2022. <https://doi.org/10.1101/2022.09.14.508057>.
- Jääntti H, Sitnikova V, Ishchenko Y, Shakirzyanova A, Giudice L, Ugidos IF, et al. Microglial amyloid beta clearance is driven by PIEZO1 channels. *J Neuroinflammation*. 2022;19(1):147.
- Oksanen M, Petersen AJ, Naumenko N, Puttonen K, Lehtonen Š, Gubert Olivé M, et al. PSEN1 Mutant iPSC-Derived model reveals severe astrocyte pathology in Alzheimer's disease. *Stem Cell Rep*. 2017;9(6):1885–97.
- Oksanen M, Hyötyläinen I, Voutilainen J, Puttonen KA, Hämäläinen RH, Graff C, et al. Generation of a human induced pluripotent stem cell line (LL008.1.4) from a familial Alzheimer's disease patient carrying a double KM670/671NL (Swedish) mutation in APP gene. *Stem Cell Res*. 2018;31:181–5.
- Kontinen H, Cabral-da-Silva MC, Ohtonen S, Wojciechowski S, Shakirzyanova A, Caligola S, et al. PSEN1ΔE9, APPsw, and APOE4 confer disparate phenotypes in human iPSC-derived microglia. *Stem Cell Rep*. 2019;13(4):669–83.
- Frederiksen HR, Holst B, Ramakrishna S, Muddashetty R, Schmid B, Freude K. Generation of two iPSC lines with either a heterozygous V717I or a heterozygous KM670/671NL mutation in the APP gene. *Stem Cell Res*. 2019;34: 101368.
- Korhonen H, Kanninen KM, Lehtonen Š, Lemarchant S, Puttonen KA, Oksanen M, et al. Immunomodulation by interleukin-33 is protective in stroke through modulation of inflammation. *Brain Behav Immun*. 2015;49:322–36.
- Weltner J, Balboa D, Katayama S, Bespalov M, Krjutškov K, Jouhilahti EM, et al. Human pluripotent reprogramming with CRISPR activators. *Nat Commun*. 2018;9(1):2643.
- Sokka J, Yoshihara M, Kvist J, Laiho L, Warren A, Stadelmann C, et al. CRISPR activation enables high-fidelity reprogramming into human pluripotent stem cells. *Stem Cell Rep*. 2022;17(2):413–26.
- Blanchard JW, Bula M, Davila-Velderrain J, Akay LA, Zhu L, Frank A, et al. Reconstruction of the human blood–brain barrier *in vitro* reveals a pathogenic mechanism of APOE4 in pericytes. *Nat Med*. 2020;26(6):952–63.
- Wang K, Lin RZ, Hong X, Ng AH, Lee CN, Neumeyer J, et al. Robust differentiation of human pluripotent stem cells into endothelial cells via temporal modulation of ETV2 with modified mRNA. *Sci Adv*. 2020;6:30.
- Deli MA, Ábrahám CS, Kataoka Y, Niwa M. Permeability studies on *in vitro* blood–brain barrier models: physiology, pathology, and pharmacology. *Cell Mol Neurobiol*. 2005;25(1):59–127.
- Takata F, Dohgu S, Yamauchi A, Matsumoto J, Machida T, Fujishita K, et al. *In vitro* blood–brain barrier models using brain capillary endothelial cells isolated from neonatal and adult rats retain age-related barrier properties. *PLoS ONE*. 2013;8:1.
- Neuhaus AA, Couch Y, Sutherland BA, Buchan AM. Novel method to study pericyte contractility and responses to ischaemia *in vitro* using electrical impedance. *J Cereb Blood Flow Metab*. 2017;37(6):2013–24.
- Hibbs E, Love S, Miners JS. Pericyte contractile responses to endothelin-1 and Aβ peptides: assessment by electrical impedance assay. *Front Cell Neurosci*. 2021;20(15): 723953.
- Koskivi M, Pörsti E, Hewitt T, Räsänen N, Wu Y-C, Trontti K. Genetic contribution to microglial activation in schizophrenia. *Molecular Psychiatry*. 2024. <https://doi.org/10.1038/s41380-024-02529-1>.
- Dobin A, Davis CA, Schlesinger F, Drenkow J, Zaleski C, Jha S, et al. STAR: ultrafast universal RNA-seq aligner. *Bioinformatics*. 2013;29(1):15–21.

30. Anders S, Pyl PT, Huber W. HTSeq—a Python framework to work with high-throughput sequencing data. *Bioinformatics*. 2015;31(2):166–9.
31. Love MI, Huber W, Anders S. Moderated estimation of fold change and dispersion for RNA-seq data with DESeq2. *Genome Biol*. 2014;15(12):550.
32. Ma Q, Zhao Z, Sagare AP, Wu Y, Wang M, Owens NC, et al. Blood-brain barrier-associated pericytes internalize and clear aggregated amyloid- β 42 by LRP1-dependent apolipoprotein E isoform-specific mechanism. *Mol Neurodegener*. 2018;13(1):57.
33. Shi H, Koronyo Y, Rentsendorj A, Regis GC, Sheyn J, Fuchs DT, et al. Identification of early pericyte loss and vascular amyloidosis in Alzheimer's disease retina. *Acta Neuropathol (Berl)*. 2020;139(5):813–36.
34. Zhang Y, Sloan SA, Clarke LE, Caneda C, Plaza CA, Blumenthal PD, et al. Purification and characterization of progenitor and mature human astrocytes reveals transcriptional and functional differences with mouse. *Neuron*. 2016;89(1):37–53.
35. Donato AJ, Lesniewski LA, Stuart D, Walker AE, Henson G, Sorensen L, et al. Smooth muscle specific disruption of the endothelin-A receptor in mice reduces arterial pressure, and vascular reactivity and affects vascular development. *Life Sci*. 2014;118(2):238–43.
36. Li A, Dubey S, Varney ML, Dave BJ, Singh RK. IL-8 directly enhanced endothelial cell survival, proliferation, and matrix metalloproteinases production and regulated angiogenesis. *J Immunol*. 2003;170(6):3369–76.
37. De Heer EC, Jalving M, Harris AL. HIFs, angiogenesis, and metabolism: elusive enemies in breast cancer. *J Clin Invest*. 2020;130(10):5074–87.
38. Yu Y, Leng Y, Song X, Mu J, Ma L, Yin L, et al. Extracellular matrix stiffness regulates microvascular stability by controlling endothelial paracrine signaling to determine pericyte fate. *Arterioscler Thromb Vasc Biol*. 2023;43(10):1887–99.
39. Smyth LCD, Rustenhoven J, Park TH, Schweder P, Jansson D, Heppner PA, et al. Unique and shared inflammatory profiles of human brain endothelia and pericytes. *J Neuroinflammation*. 2018;15(1):138.
40. Navarro R, Compte M, Álvarez-Vallina L, Sanz L. Immune regulation by pericytes: modulating innate and adaptive immunity. *Front Immunol*. 2016;7:480.
41. Kelleher J, Dickinson A, Cain S, Hu Y, Bates N, Harvey A, et al. Patient-specific iPSC model of a genetic vascular dementia syndrome reveals failure of mural cells to stabilize capillary structures. *Stem Cell Rep*. 2019;13(5):817–31.
42. Evensen L, Micklem DR, Blois A, Berge SV, Aarsæther N, Littlewood-Evans A, et al. Mural cell associated VEGF is required for organotypic vessel formation. *PLoS ONE*. 2009;4(6):e5798.
43. Kalaria RN, Premkumar DR, Pax AB, Cohen DL, Lieberburg I. Production and increased detection of amyloid β protein and amyloidogenic fragments in brain microvessels, meningeal vessels and choroid plexus in Alzheimer's disease. *Mol Brain Res*. 1996;35(1–2):58–68.
44. Natté R, De Boer WI, Maat-Schieman MLC, Baelde HJ, Vinters HV, Roos RAC, et al. Amyloid β precursor protein-mRNA is expressed throughout cerebral vessel walls. *Brain Res*. 1999;828(1–2):179–83.
45. Greenberg SM, Bacskai BJ, Hernandez-Guillamon M, Pruzin J, Sperling R, van Veluw SJ. Cerebral amyloid angiopathy and Alzheimer disease — one peptide, two pathways. *Nat Rev Neurol*. 2020;16(1):30–42.
46. Beamish JA, He P, Kottke-Marchant K, Marchant RE. Molecular regulation of contractile smooth muscle cell phenotype: implications for vascular tissue engineering. *Tissue Eng Part B Rev*. 2010;16(5):467–91.
47. Hillsley A, Santos JE, Rosales AM. A deep learning approach to identify and segment alpha-smooth muscle actin stress fiber positive cells. *Sci Rep*. 2021;11(1):21855.
48. Chow N, Bell RD, Deane R, Streb JW, Chen J, Brooks A, et al. Serum response factor and myocardin mediate arterial hypercontractility and cerebral blood flow dysregulation in Alzheimer's phenotype. *Proc Natl Acad Sci*. 2007;104(3):823–8.
49. Alarcon-Martinez L, Yilmaz-Ozcan S, Yemisci M, Schallek J, Kılıç K, Can A, et al. Capillary pericytes express α -smooth muscle actin, which requires prevention of filamentous-actin depolymerization for detection. *Elife*. 2018;21(7):e34861.
50. Cheresch DA, Leng J, Klemke RL. Regulation of cell contraction and membrane ruffling by distinct signals in migratory cells. *J Cell Biol*. 1999;146(5):1107–16.
51. Ihara E, Yu Q, Chappellaz M, MacDonald JA. ERK and p38 MAPK pathways regulate myosin light chain phosphatase and contribute to Ca^{2+} sensitization of intestinal smooth muscle contraction. *Neurogastroenterol Motil*. 2015;27(1):135–46.
52. Nortley R, Korte N, Izquierdo P, Hirunpattarasilp C, Mishra A, Jaunmuktane Z, et al. Amyloid β oligomers constrict human capillaries in Alzheimer's disease via signaling to pericytes. *Science*. 2019;365:6450.
53. Hartz AMS, Bauer B, Soldner ELB, Wolf A, Boy S, Backhaus R, et al. Amyloid- β contributes to blood-brain barrier leakage in transgenic human amyloid precursor protein mice and in humans with cerebral amyloid angiopathy. *Stroke*. 2012;43(2):514–23.
54. Weiss N, Miller F, Cazaubon S, Couraud PO. The blood-brain barrier in brain homeostasis and neurological diseases. *Biochim Biophys Acta BBA - Biomembr*. 2009;1788(4):842–57.
55. Gerszten RE, Garcia-Zepeda EA, Lim YC, Yoshida M, Ding HA, Gimbrone MA, et al. MCP-1 and IL-8 trigger firm adhesion of monocytes to vascular endothelium under flow conditions. *Nature*. 1999;398(6729):718–23.
56. Yao Y, Tsirka SE. Monocyte chemoattractant protein-1 and the blood-brain barrier. *Cell Mol Life Sci*. 2014;71(4):683–97.
57. Sun Y, Li N, Zhang J, Liu H, Liu J, Xia X, et al. Enolase of streptococcus Suis serotype 2 enhances blood-brain barrier permeability by inducing IL-8 release. *Inflammation*. 2016;39(2):718–26.
58. Zegeye MM, Andersson B, Sirsjö A, Ljungberg LU. IL-6 trans-signaling impairs sprouting angiogenesis by inhibiting migration, proliferation and tube formation of human endothelial cells. *Cells*. 2020;9(6):1414.
59. Bharti R, Dey G, Das AK, Mandal M. Differential expression of IL-6/IL-6R and MAO-A regulates invasion/angiogenesis in breast cancer. *Br J Cancer*. 2018;118(11):1442–52.
60. Gu C, Lhamo T, Zou C, Zhou C, Su T, Draga D, et al. Comprehensive analysis of angiogenesis-related genes and pathways in early diabetic retinopathy. *BMC Med Genomics*. 2020;13(1):142.
61. Xu H, Pumiglia K, LaFlamme SE. Laminin-511 and $\alpha 6$ integrins regulate the expression of CXCR4 to promote endothelial morphogenesis. *J Cell Sci*. 2020. <https://doi.org/10.1242/jcs.246595>.

Publisher's Note

Springer Nature remains neutral with regard to jurisdictional claims in published maps and institutional affiliations.